# Semi-Analytical Model for Superelastic Behavior of Twisted SMA Microfilament Yarns

Charles A. Weinberg, Song Cai, Jeremy Schaffer, Julianna Abel\*

[\*] Prof. Julianna Abel Corresponding-Author, Charles Weinberg Mechanical Engineering Department, University of Minnesota, Minneapolis, Minnesota 55405, USA

E-mail: jabel@umn.edu

Dr. Jeremy Schaffer, Dr. Song Cai, Research and Development, Fort Wayne Metals, Fort Wayne, Indiana 46809, USA

#### 1. Abstract

Manufacturing improvements have enabled the integration of shape memory alloys (SMA) into novel form factors to offer tailored solutions to engineering applications. Of these form factors, multifunctional twisted SMA microfilament yarns offer tailorable superelastic behavior, improved actuation displacements, and increased flexibility for integration within textiles for medical devices, defense structures, and wearable technologies. However, the lack of understanding of the underlying physics of twisted SMA yarns limits the potential in functionalized SMA textiles. This paper develops a semi-analytical model of the micro-scale mechanics of superelastic SMA twisted yarns to predict their macroscopic mechanical behavior. Using traditional yarn models redefined within SMA constitutive equations, the evolution of material phases of the microfilaments within the mesoscale yarn element is tracked to the predicted macroscale yarn force. Through validation, the functional dependence of the yarn response, including effective modulus and phase transition dynamics, on twist is predicted by the model. The model fills a knowledge gap necessary for manufacturing SMA yarns with desired mechanical characteristics, limiting application strains to avoid failure, and achieving consistent cycled behavior. The model provides a framework for modeling the shape memory effect in SMA microfilament yarns and establishes an understanding of SMA yarns for implementation within textile models.

#### 2. Introduction

Advancements in manufacturing capabilities have enabled researchers to integrate multifunctional materials, such as shape memory alloys (SMA), in novel form factors to offer tailored solutions to real engineering applications [1]-[8]. Of these novel form factors, twist inserted structures offer unique rotational motions, improved actuation displacements, tailorable moduli, adjustable hysteresis, and increased flexibility, motivating researchers to integrate SMA within a twisted structure. For example, SMA torque tubes offer rotary actuation for increased control over wing tip dynamics in aerospace applications [9]. SMA wire ropes and cables demonstrate superelastic capabilities in a robust structure for structural applications [10]-[11]. Scaling down to moderate filament diameters, Kianzad et al. [12] demonstrated both linear and rotational actuation in a NiTi wire twisted structure. Leveraging the enhanced flexibility of twisted structures, Granberry et al. [13] integrated a NiTi wire twisted structure in textiles capable of auxetic actuation. While promising, these relatively large diameter and low filament count structures are still too rigid to produce cloth-like textiles. Until recently, the ability to manufacture large numbers of small diameter NiTi filaments for yarn manufacturing did not exist. Our previous

research [14] highlighted such manufacturing advancements, demonstrated an improved tunability of traditional SMA and SE behavior in the yarn structure experimentally, and displayed the potential of yarns in a cloth-like textile. However, without an understanding of the underlying physics, the tailorability of NiTi microfilament twisted yarns is limited in scope, and the potential in textiles remains unrealized.

The yarn structure alters, enhances, or maintains desirable material properties in a compliant form that is useful independently or integrated within a textile for engineering applications [15]-[19]. Understanding yarn behavior facilitates the design, manufacturing, and control of a functionalized system. Modeling the underlying physics of yarn extensional behavior is done in three distinct methods: energy derived [20]-[21], finite element [22]-[23], and equilibrium assumptions [24]-[25]. Energy derived methods use filament stress-strain curves of conventional engineering materials to predict global yarn behavior through strain energy theorems. While energy methods account for nonlinear materials and large extensions, they provide no information on the microfilament stress-strain states, limiting tunable design to a black-box approach. Finite element methods are powerful modeling tools that account for nonlinear materials and microfilament stress and strains, but they are computationally expensive and limit real-time adjustments and the total number of simulations. The oldest method, popularized by J.W.S Hearle [15], uses linear elastic materials with governing yarn equilibrium assumptions to map microfilament mechanisms to macro-yarn extensional behavior. This method is computationally inexpensive and provides insights into the stress state of the microfilament, but the linear elastic assumption limits the use of this structural model with most multifunctional material models.

Numerous SMA materials models have been derived to 1) comprehend underlying physics and mechanisms, 2) identify material or processing parameters, or 3) predict the material response to aid in application development and integration [26]. Thorough reviews of SMA material models [26]-[30] highlight there are been two major branches; microscopic and macroscopic. The microscopic approach has yielded strong results for understanding physics and identifying important parameters in SMA material modeling [31]-[32], but has proven to be mathematically rigorous and computationally expensive to predict the material response for real engineering applications. On the other hand, the macroscopic approach has yielded strong results for predicting the SMA material response on the larger, macroscopic scale [33]-[37]. This approach is less computationally intensive, providing more simulations and real-time information to control SMA integrated systems better. Of the macroscopic approaches, most fall under the category of phenomenological models that use a thermodynamic principle framework, or in this work, a free energy basis, to describe the material response. Phenomenological models navigate the stress-straintemperature relationship of SMAs by defining the driving forces and evolution of internal state variables such as a martensitic volume fraction. Researchers have implemented phenomenological models in a variety of ways, with one of the most popular phenomenological models is a one-dimensional model developed by Brinson [33]. However, as SMA integrated systems have grown in complexity, so has the need for more robust multi-axial models. To account for multi-axial loading scenarios, many have utilized finite element methods [38]-[40], but this limits the number of simulations that can be performed. Others have been able to reduce their models to exact solutions [41], but this is not possible for every modeling scenario. When exact solutions are not achievable, and computer laboring FEM methods are to be avoided, semi-analytical solutions [42]-[43] are frequently employed.

This paper presents a model of the micro-scale mechanics of superelastic NiTi microfilament twisted yarns to predict their macroscopic mechanical behavior. The model modifies existing structural and material models to interoperate and capture the nonlinear mechanics in both the yarn geometry and SMA material. Insight into microfilament response is provided by Hearle's linear elastic yarn equilibrium model [15], which is expanded with the 3D phenomenological SMA material model from Boyd & Lagoudas

[44] and Qidwai and Lagoudas [45]. This paper utilizes a semi-analytical framework modified from Andani & Elahinia [46]. For yarn extension, the material phases of the microfilaments are identified using a martensite volume fraction, and the filament stress and strains are calculated from combined material and yarn equations. Common loading and unloading material phase evolutions are outlined in the context of the microfilament kinematics and mapped to the macro yarn force response. To validate the model, the macro yarn force response is compared with experimental data for five yarn variations. The model predicts the relationship between twist and mechanical characteristics such as effective modulus, phase transitions, and loading/unloading asymmetry. The combined model predicts global yarn superelastic response by capturing SMA microfilament stresses – filling a knowledge gap necessary for tailorable design and functionalized integration of SMA microfilament yarns in SMA textiles.

#### 3. Yarn Mechanics

Yarn theory is an established field, and much of this work builds on relationships defined in *Structural Mechanics of Fibers, Yarns, and Fabrics* written by J.W.S Hearle [15]. In this model, the complex filament pathways within yarns are simplified to a helical geometry to create a microscopic yarn geometry. The microfilaments are then grouped within a mesoscopic yarn element, where governing equations are derived by mapping filament strains to stresses. Lastly, the mesoscopic contributions are scaled up to a macroscopic yarn force to complete the hierarchical analysis. Simplifying the filament and yarn geometry enables relationships to be defined from macroscopic yarn extension to microscopic filament strain and scaled back up to macroscopic yarn force.

#### 3.1. Macroscopic Yarn Geometry

The macroscopic geometry of continuous filament (CF) yarns comprises the microscopic geometry of the constitutive filaments. In the simplest theory, each filament in the yarn is modeled as an idealized helical structure (Figure 1). In the idealized helical structure, each filament follows a uniform helical path geometrically defined by a constant radius, r, from the yarn axis and constant helical angle,  $\theta$ , and a helical pitch, h. Unraveling one turn of the helix makes it easy to visualize the helical pitch, h, as well as the filament length in one turn of twist, l (Figure 1). The helical radius, r, varies from zero at the center of the yarn (Figure 1a) to the yarn radius,  $R_y$ , at the surface of the yarn (Figure 1b). Similarly, the helical angle,  $\theta$ , will vary from zero at the center of the yarn to the surface twist angle,  $\alpha$ , at the surface and the length in one turn of twist, l, varies from the helical pitch, h, at the center to the length in one turn of twist at the surface, L. Unlike the other parameters, it is assumed that all filaments share a common helical pitch, h, defined as

$$h = \frac{1}{\beta}.$$
 (Eq.1)

The yarn twist,  $\beta$ , is a controllable manufacturing parameter estimated from the angular spindle speed,  $W_s$ , and the linear delivery speed,  $V_d$ , to be

$$\beta \cong \frac{W_s}{V_d}.$$
 (Eq.2)

In addition to defining the helical pitch, yarn twist,  $\beta$ , is one of three global yarn parameters needed to quantify the yarn radius,  $R_y$ , and surface twist angle,  $\alpha$ . The yarn count, C, or linear density, is used to quantify the amount of active material in the yarn across different bundle configurations and is defined as

$$C[tex] = n(\rho \pi r_f^2) * 10^5.$$
 (Eq.3)

Where the number of filaments, n, the density of the filament material,  $\rho$ , and the filament radius,  $r_f$ , are also controllable manufacturing decisions. The unit tex is a standard industry term and is defined as the mass, in grams, in 1000 meters of yarn. The last global yarn parameter needed is the packing density,  $\varphi$ , which describes the efficiency of the filaments to pack within the yarn geometry, using the specific volumes of the fibers,  $\omega_f$ , and the yarn,  $\omega_{\gamma}$ , and is defined as

$$\varphi = \frac{\omega_f}{\omega_v}.$$
 (Eq.4)

Together, yarn count, C, yarn twist,  $\beta$ , and packing density,  $\varphi$ , provide a theoretical foundation to relate the controllable processing of CF yarn structures to the global geometry of the yarn by defining the yarn radius,  $R_{\gamma}$ , and surface twist angle,  $\alpha$ , as

$$R_{y} = \sqrt{\frac{\omega_{y}C}{10^{5}\pi}}$$
 (Eq.5)

$$tan(\alpha) = 0.0112 \cdot \beta \cdot \sqrt{C} \cdot \sqrt{\omega_{y}}.$$
 (Eq.6)

## 3.2. Macroscopic Yarn Extension

When yarn is extended by a global yarn strain,  $\varepsilon_y$ , the constitutive filament helixes change pitch, length, and radius  $(\delta h, \delta l, \delta r)$ , as seen in Figure 1c. The yarn structural engineering strain,  $\varepsilon_y$ , is related to the change in helical pitch, h, through

$$\varepsilon_y = \frac{\delta h}{h}.$$
 (Eq.7)

However, the change in radius and filament length need further consideration. Under an axial yarn strain, the yarn will undergo a radial contraction that is assumed to be fractionally distributed uniformly across all filaments in the yarn. The change in yarn radius is defined by introducing a yarn lateral contraction ratio,  $v_y$ , similar to a natural Poisson's ratio, v, and defined as

$$v_{y} = -\frac{\frac{\delta R}{R}}{\frac{\delta h}{h}} = -\frac{\frac{\delta r}{r}}{\frac{\delta h}{h}} = -\frac{h}{r}\frac{\delta r}{\delta h}.$$
 (Eq.8)

Unless the yarn contraction behavior is known, it is simple and reasonable to assume the yarn contracts at a constant yarn volume (i.e.  $v_y = 0.5$ ).

Revisiting the unraveled geometry in Figure 1, a Pythagoras relationship between the filament length, helical pitch, and radius exists. Differentiating, rearranging, and substituting in (Eq.8) yields the axial filament strain.

$$\varepsilon_f = \varepsilon_y \left( \frac{c^2}{u^2} - v_y \left( 1 - \frac{c^2}{u^2} \right) \right),$$
 (Eq.9)

where c is the twist constant and is used to indicate the level of yarn twist, and u is the filament length ratio, which is a measure of radial position and varies from c at the center of the yarn to one at the surface. Both are defined as,

$$c = \cos(\alpha) = h/L \tag{Eq.10}$$

$$u = \frac{l}{L}. (Eq.11)$$

For a given yarn strain,  $\varepsilon_y$ , the filament strain,  $\varepsilon_f$  (Eq. 9), is at a minimum at the outer surface of the yarn, where the contribution of radial contraction is at a maximum. Mechanically, radial contraction reduces the direct conversion of yarn strain to axial filament strain through rigid body motion in the helical geometry. Conversely, the axial filament strain,  $\varepsilon_f$ , is a maximum at the center of the yarn where the filament length ratio, u, approaches the twist constant, c, and the contribution of axial filament strain from radial contraction (Eq. 9) approaches zero.

#### 3.3. Mesoscopic Yarn Element

The filament strains are related to stresses through a yarn element (Figure 2) defined by Hearle [15]. A small element is taken between two radial positions separated by a radial thickness, dr, an angular change,  $d\phi$ , from the helical pitch,  $\theta$ , and a length, dz, along the yarn axis. It is assumed the element is composed of enough infinitesimally small filaments where considering the individual arrangements is not necessary. The shear, torsional, and bending moments acting on the yarn element are infinitesimally small and, therefore, neglected. The remaining forces acting on the element are normal to each face. Two equal axial stresses, X, act outward in directions parallel to the fiber axis on the axial face's ABCD and EFGH. Two compressive stresses, G, act on tangential faces ADHE and BCGF. Lastly, there are two compressive stresses, G, acting on radial faces GF and GF and GF and GF are assumed to be equal, creating a hydrostatic condition on the element. The hydrostatic assumption is based on the explanation that the filaments will reconfigure to equalize the stresses across opposite faces. Conventional sign convention, tension is positive and compression is negative, is employed throughout the development of this work.

## 3.4. Mesoscopic Yarn Equilibrium

From symmetry, the axial stresses, X, and areas on the two axial end faces, ABCD and EFGH, are equal, thus the forces across these faces,  $N_{ABCD}$  and  $N_{EFGH}$ , are equal and expressed as

$$N_{ABCD} = N_{EFGH} = X * area(ABCD) = Xrcos(\theta)d\phi dr.$$
 (Eq.12)

Similarly, the tangential stresses, G, and areas on the tangential faces, ADHE and BCGF, are equal, thus the forces across these faces,  $N_{ADHE}$  and  $N_{BCGF}$ , are equal and expressed as

$$N_{ADHE} = N_{BCGE} = -G * area(ADHE) = -Gsec(\theta)drdz.$$
 (Eq.13)

In the radial direction, the radial stress, G, and area of the faces vary with the helical radius, r. The force,  $N_{ABFE}$ , across ABFE is

$$N_{ABFE} = -G * area(ABFE) = -Grd\phi dz.$$
 (Eq.14)

While the force,  $N_{DCGH}$ , across the opposite face DCGH is

$$N_{DCGH} = -Grd\phi dz - \left(G + r\frac{dG}{dr}\right)drd\phi dz. \tag{Eq.15}$$

However, to satisfy equilibrium in the radial direction, the sum of the forces acting on the yarn element in the radial direction must be equal to zero. Three forces make up that equilibrium:

- 1) a radially compressive component from the filament tension, caused by the difference in the direction of the forces on the axial faces from the helix,
- 2) a radially outward component from the faces of ADHE and BCGF belonging to a helix, and
- 3) the force differential between  $N_{ABFE}$  (Eq.14) and  $N_{DCGH}$  (Eq.15).

Simplifying the radial components yields a single ordinary differential equation that governs radial equilibrium as a function of filament length ratio, u (Eq. 11). It is expressed as

$$\frac{dG}{du} = \frac{X - G}{u}.$$
 (Eq.16)

With the boundary condition that the tangential stress, G, at the surface of the yarn is zero (G(1) = 0). With the adopted sign convention, a positive axial stress, X, and negative compressional tangeital stress, G, leads to a positive quantity for X - G, and thus the radial equilibrium ODE (Eq.16).

#### 3.5. Macroscopic Yarn Tension

For a yarn under extension, each yarn element contributes a force component, f, to the global yarn force, F, along the yarn axis. The elemental contribution, f, is composed of the filament axial stress, X, and the tangential stress, G, but not the radial stress, G, and is expressed as

$$f = X(2\pi r dr cos(\theta))\cos(\theta) + G(2\pi r dr sin(\theta))\sin(\theta).$$
 (Eq.17)

The yarn force, F, is calculated from a summation of those components across the yarn radius normalized by the packing density. After substituting, this yields

$$F = \varphi \frac{2\pi R_y^2}{1 - c^2} \int_c^1 \left[ X \frac{c^2}{u^2} + G \left( 1 - \frac{c^2}{u^2} \right) \right] u du.$$
 (Eq.18)

#### 4. 3D Constitutive SMA Material Model

During yarn extension, the individual filaments within the yarn element experience tension along the filament axis and compression in the orthogonal directions, requiring a material model capable of handling multi-axial loading. The model chosen is a 3D phenomenological constitutive model for SMAs

developed by Boyd and Lagoudas [40] and Qidwai and Lagoudas [45]. The model provides a robust 3D framework for applying specific combined loading scenarios, such as the combined tension-torsion loading of an SMA rod seen in Andani and Elahnia [46]. In this work, the combined tension-compression loading of the yarn element is applied within the phenomenological constitutive model. The model has multiple features that are vital for current simulations and future improvements. The model can consider non-proportional loading [42], experimentally derived hardening functions [47], different forms of equivalent stresses to account for tension-compression asymmetry [48], and plastic yielding [49]. Lastly, the model has a Gibbs free energy basis which allows for strain-controlled simulations that align with traditional yarn experimental procedures, compared with Hemholtz free energy models [37] that represent results in the strain-temperature domain. The total Gibbs free energy, Γ, of polycrystalline SMA is defined as

$$\Gamma = -\frac{1}{2\rho}\sigma : S : \sigma - \frac{1}{\rho}\sigma$$

$$: \left[a(T - T_0) + \varepsilon^t\right] + b\left[(T - T_0) - T\ln\left(\frac{T}{T_0}\right)\right] - s_0T + \eta_0 + \frac{1}{\rho}f(\xi). \tag{Eq.19}$$

The Gibbs free energy,  $\Gamma$ , is a function of internal state variables,  $\sigma$ ,  $\varepsilon^t$ , T,  $T_0$ , and  $\xi$ , which are the Cauchy stress tensor, transformation strain tensor, temperature, reference temperature, and martensitic volume fraction. The material constants, S,  $\rho$ , a, b,  $s_0$ , and  $\eta_0$ , are the effective compliance tensor, density, effective thermal expansion coefficient tensor, effective specific heat, effective specific entropy at the reference state, and the effective specific internal energy at the reference state. The effective material properties are defined by the martensitic volume fraction,  $\xi$ , and the rule of mixtures. For example, the effective compliance tensor is expressed as

$$S = S^A + \xi(S^M - S^A).$$
 (Eq.20)

The remaining parameter in (Eq.19),  $f(\xi)$ , is the transformation strain hardening function and is modeled with a quadratic dependence [42] on martensitic volume fraction,  $\xi$ , and expressed as

$$f(\xi) = \begin{cases} \frac{1}{2}\rho q^{M}\xi^{2} + (\mu_{1} + \mu_{2})\xi; & \dot{\xi} > 0\\ \frac{1}{2}\rho q^{A}\xi^{2} + (\mu_{1} - \mu_{2})\xi; & \dot{\xi} < 0 \end{cases}$$
(Eq.21)

Where  $\rho q^M$ ,  $\rho q^A$ ,  $\mu_1$ , and  $\mu_2$  are model paramaters that are determined experimentally and defined in Eq.S1 (Supporting Information). Using Gibbs free energy,  $\Gamma$  (Eq.19), within the first law of thermodynamics, a constitute relation for strain,  $\varepsilon$ , is expressed as

$$\varepsilon = -\rho \frac{d\Gamma}{d\sigma} = S : \sigma + a(T - T_0) + \varepsilon^t.$$
 (Eq.22)

For superelastic loading, it is assumed that any change in the system comes as a result of a change in martensitic volume fraction,  $\xi$ . To relate the evolution of the transformation strain tensor,  $\varepsilon^t$  to the evolution of the martensitic volume fraction,  $\dot{\xi}$ , the following relation is defined:

$$\dot{\varepsilon^t} = \Lambda^t \dot{\xi}. \tag{Eq.23}$$

The transformation tensor,  $\Lambda^t$ , governs the direction of the transformation strain and is expressed as

$$\Lambda^{t} = \begin{cases} \frac{3}{2} H \frac{\sigma'}{\bar{\sigma}}, & \dot{\xi} > 0\\ \frac{\varepsilon^{t-r}}{\bar{\xi}^{t-r}}, & \dot{\xi} < 0 \end{cases}$$
 (Eq.24)

where H is a material property called the maximum uniaxial transformation strain at full transformation and is determined experimentally. The effective stress,  $\bar{\sigma}$ , is defined as the von Mises equivalent stress,

$$\bar{\sigma} = \sqrt{\frac{3}{2}\sigma':\sigma'},\tag{Eq.25}$$

and  $\sigma'$  is the deviatoric stress tensor. As seen in (Eq.24), the forward transformation, defined as the solid-state material phase transformation from austenite (A) to stressed induced martensite (SIM, M<sup>+</sup>), is guided by the applied deviatoric stress,  $\sigma'$ . For reverse transformation, defined as the opposite transformation from SIM back to austenite, the orientation is governed by the ratio of the forward transformation strain at reversal,  $\varepsilon^{t-r}$ , to the martensitic volume fraction at reversal,  $\xi^{t-r}$ .

Using the second law of thermodynamics, the total dissipation rate is written as

$$\sigma : \varepsilon^t - \rho \frac{d\Gamma}{d\xi} = \Pi \dot{\xi} \ge 0, \tag{Eq.26}$$

where  $\Pi$  is the thermodynamic force and is expressed as

$$\Pi = \sigma : \Lambda^{t} + \frac{1}{2}\sigma : \Delta S : \sigma + \Delta a$$

$$: \sigma(T - T_{0}) - \rho \Delta b \left[ (T - T_{0}) - T \ln \left( \frac{T}{T_{0}} \right) \right] + \rho \Delta s_{0} T - \frac{df}{d\xi} - \rho \Delta \eta_{0}.$$
(Eq.27)

In this equation, the symbol  $\Delta$ , shown before a variable, denotes the change in that variable from the martensitic to austenitic phases ( $\Delta p = p^M - p^A$ ).

The transformation function,  $\Phi$ , defines the start and length of the transformations from a relationship between the thermodynamic force,  $\Pi$ , and the internal energy dissipated, Y (Eq.S1), during solid-state phase transformation:

$$\Phi(\sigma, T, \xi) = \begin{cases}
\Pi - Y^{fwd} = 0, & \dot{\xi} > 0 \\
-\Pi - Y^{rev} = 0, & \dot{\xi} < 0. \\
< 0, & \dot{\xi} = 0
\end{cases}$$
(Eq.28)

When  $\Phi < 0$ , the material is in the elastic domain (austenite or stressed-induced martensite), and the martensitic volume fraction is not changing ( $\dot{\xi} = 0$ ). During forward and reverse transformation, the stress, temperature, and martensitic volume fraction are constrained on the transformation surface where  $\Phi = 0$ .

## 5. Constitutive equations of multi-axial loading of SMA yarn element

The yarn element derived in Sec. 3.3 has stress and strain tensors with the following forms,

$$\sigma = \begin{pmatrix} G & 0 & 0 \\ 0 & G & 0 \\ 0 & 0 & X \end{pmatrix}, \varepsilon = \begin{pmatrix} \varepsilon_{rr} & 0 & 0 \\ 0 & \varepsilon_{\phi\phi} & 0 \\ 0 & 0 & \varepsilon_f \end{pmatrix} = \begin{pmatrix} \varepsilon_t & 0 & 0 \\ 0 & \varepsilon_t & 0 \\ 0 & 0 & \varepsilon_f \end{pmatrix},$$

$$\varepsilon^{t-r} = \begin{pmatrix} \varepsilon_t^{t-r} & 0 & 0 \\ 0 & \varepsilon_t^{t-r} & 0 \\ 0 & 0 & \varepsilon_f^{t-r} \end{pmatrix}.$$
(Eq.29)

Using the yarn element's stress tensor,  $\sigma$ , the deviatoric stress tensor,  $\sigma'$ , is expressed as

$$\sigma' = \begin{pmatrix} -\frac{X-G}{3} & 0 & 0\\ 0 & -\frac{X-G}{3} & 0\\ 0 & 0 & \frac{2(X-G)}{3} \end{pmatrix}$$
 (Eq.30)

and the von Mises equivalent stress (Eq.25) is solved to be

$$\bar{\sigma} = X - G. \tag{Eq.31}$$

The transformation tensor (Eq.24) is expanded and simplified to

$$\Lambda_{fwd}^{t} = \frac{3H}{2(X-G)} \begin{pmatrix} -\frac{X-G}{3} & 0 & 0 \\ 0 & -\frac{X-G}{3} & 0 \\ 0 & 0 & \frac{2(X-G)}{3} \end{pmatrix} = \begin{pmatrix} -\frac{1}{2} & 0 & 0 \\ 0 & -\frac{1}{2} & 0 \\ 0 & 0 & 1 \end{pmatrix} \\
\Lambda_{rev}^{t} = \frac{1}{\xi^{t-r}} \begin{pmatrix} \varepsilon_{t}^{t-r} & 0 & 0 \\ 0 & \varepsilon_{t}^{t-r} & 0 \\ 0 & 0 & \varepsilon_{f}^{t-r} \end{pmatrix} = \begin{pmatrix} -\frac{1}{2} & 0 & 0 \\ 0 & -\frac{1}{2} & 0 \\ 0 & 0 & 1 \end{pmatrix}, \tag{Eq.32}$$

where the transformation strains at reversal are defined as

$$\varepsilon_t^{t-r} = -\frac{1}{2}H\xi^{t-r},$$

$$\varepsilon_f^{t-r} = H\xi^{t-r}.$$
(Eq.33)

The martensitic volume fraction,  $\xi$ , for the forward,  $\xi^{fwd}$ , and reverse,  $\xi^{rev}$ , transformation is obtained from substituting the transformation tensor,  $\Lambda^t$  (Eq.32), into the thermodynamic force,  $\Pi$  (Eq.27), and then into the constrained transformation function,  $\Phi = 0$  (Eq.28), yielding

$$\xi^{fwd} = \frac{1}{\rho q^M} \left[ (X - G)H + \frac{1}{2} \Delta S_{33} (-2G^2 \nu + 2G^2 - 4GX\nu + X^2) + \rho \Delta s_0 (T - M_s) + \rho \Delta b \left[ (T - T_0) - T ln \left( \frac{T}{T_0} \right) \right] \right],$$
 (Eq.34)

and

$$\xi^{rev} = \frac{1}{\rho q^A} \left[ (X - G)H + \frac{1}{2} \Delta S_{33} (-2G^2 \nu + 2G^2 - 4GX\nu + X^2) + \rho \Delta s_0 (T - A_f) + \rho \Delta b \left[ (T - T_0) - T ln \left( \frac{T}{T_0} \right) \right] \right]$$
(Eq.35)

Furthermore, by substituting the martensite volume fraction,  $\xi$  (Eq.34), and transformation tensor,  $\Lambda^t$ , in the evolution relationship described in (Eq.23), and integrating from zero to an arbitrary time, the transformation strain,  $\varepsilon^t$ , is obtained and substituted in the constitutive (Eq.22) to derive an expression for the filament axial strain:

$$\varepsilon_f = \frac{X - 2G\nu}{E^A + \xi(E^M - E^A)} + \xi H. \tag{Eq.36}$$

Together, the material derived equation for filament strain,  $\varepsilon_f$  (Eq.36), and the yarn derived equation for filament strain,  $\varepsilon_f$  (Eq.9), form a critical bridge between the two models, permitting the nonlinear material system to be integrated within the traditional yarn system.

## 6. Material phase evolution during yarn loading

During loading, filaments in superelastic SMA yarns experience a phase transformation from austenite (A), through the forward transformation (A & M<sup>+</sup>), to stressed induced martensite (M<sup>+</sup>). This transformation is radially distributed at different stages through the yarn, with each stage requiring a specific solution procedure. To predict the macroscopic behavior of SMA yarns, the phases present in the yarn need to be identified and used to solve for the stresses for each stage. While there are multiple loading evolutions possible, we will outline a common path, represented by the radial distribution of phases in the cross-section of the yarn (Figure 3), from a homogenous austenite yarn state (Figure 3a), through heterogeneous austenite and forward transformation (Figure 3b), homogenous forward transformation (Figure 3c), heterogenous forward transformation and SIM (Figure 3d), and finishing in a homogeneous SIM yarn state (Figure 3e).

## 6.1. Loading of homogeneous austenite

For the evolution outlined in Figure 3, it is assumed that in superelastic loading, the entirety of the yarn begins in a homogenous austenite condition (Figure 3a). In austenite, the transformation function,  $\Phi$  (Eq.28), remains in the elastic domain and the forward martensitic volume fraction,  $\xi^{fwd}$ , is constant at zero. The material is treated as a linear elastic isotropic material with a material modulus equal to  $E^A$ , and the material based equation for filament strain,  $\varepsilon_f$  (Eq.36), is updated to

$$\varepsilon_f = \frac{X - 2\nu G}{E^A}.\tag{Eq.37}$$

Substituting the derived yarn equation for filament strain,  $\varepsilon_f$  (Eq.9), and rearranging for the axial stress, X, yields

$$X = E^A \varepsilon_y \left[ \frac{c^2}{u^2} - \nu_y \left( 1 - \frac{c^2}{u^2} \right) \right] + 2\nu G. \tag{Eq.38}$$

Substituting the axial stress, X, in the governing ordinary differential equation (ODE) for radial equilibrium (Eq.16) and solving for the compressive stress, G, with the initial condition on the surface of the yarn, (G(1) = 0), yields

$$G = E^{A} \varepsilon_{y} u^{2\nu-1} \left[ \frac{c^{2} v_{y} - 2c^{2} v + v_{y} u^{2} + c^{2} + 2v v_{y} u^{2} - 2c^{2} v v_{y}}{u^{2\nu+1} (4v^{2} - 1)} - \frac{v_{y} + 2v v_{y} - 2c^{2} v + c^{2} v_{y} + c^{2} - 2c^{2} v v_{y}}{4v^{2} - 1} \right].$$
(Eq.39)

The compressive stress, G, is substituted back into the expression for the axial stress (Eq.38). For a given yarn strain,  $\varepsilon_y$ , and filament length ratio, u, all the stress and strains on the yarn element are known. The forward martensite volume fraction,  $\xi^{fwd}$  (Eq. 34), is calculated for all elements to check for the onset of forward transformation, when  $\xi^{fwd}$  is greater than zero.

## 6.2. Loading of heterogeneous austenite and forward transformation

When the forward martensitic volume fraction,  $\xi^{fwd}$ , is between zero and one, the yarn element is in forward transformation, and a mixture of austenite and martensite are present in the material. At this point in the loading evolution, the yarn is in a heterogeneous state of forward transformation and austenite (Figure 3b). The forward transformation will occur first in the center of yarn, where the equivalent stress is highest (Eq.31), due to the elevated filament strain and increased compressional stresses. The boundary of the forward transformation will grow outward towards the surface of the yarn. The outer portion of the yarn remaining in austenite is solved according to Sec. 6.1; however, the forward transformation portion requires independent consideration.

With a non-zero forward martensitic volume fraction,  $\xi^{fwd}$ , the axial stress, X, is expressed as

$$X = \left(\varepsilon_f - \xi^{fwd}H\right) * \left(E^A + \xi^{fwd}(E^M - E^A)\right) + 2G\nu$$
 (Eq.40)

by rearranging the filament strain,  $\varepsilon_f$  (Eq.36). To solve the governing radial equilibrium ODE (Eq.16), we need to consider the martensitic volume fraction,  $\xi^{fwd}$ , in the expression for axial stress X, which is also function of the filament length ratio, u. Rather than solving for an explicit solution for G, as we did in austenite, a system of differential equations is established. First, we must consider the differentials with respect to the filament length ratio, u, for filament strain  $\varepsilon_f$  (Eq.9),

$$\frac{d\varepsilon_f}{du} = \varepsilon_y \left( \frac{-2c^2}{u^3} - \nu_y \frac{2c^2}{u^3} \right), \tag{Eq.41}$$

martensitic volume fraction (Eq.34),

$$\frac{d\xi^{fwd}}{du} = \frac{1}{\rho q^M} \left[ \left( \frac{dX}{du} - \frac{dG}{du} \right) H + \frac{1}{2} \Delta S_{33} \left( -4\nu G \frac{dG}{du} + 4G \frac{dG}{du} - 4\nu G \frac{dX}{du} - 4\nu X \frac{dG}{du} + 2X \frac{dX}{du} \right) \right],$$
(Eq.42)

and axial stress (Eq.40),

$$\frac{dX}{du} = \left(\frac{d\varepsilon_f}{du} - \frac{d\xi^{fwd}}{du}H\right) \left(E^A + \xi^{fwd}(E^M - E^A)\right) + \frac{d\xi^{fwd}}{du}(E^M - E^A) \left(\varepsilon_f - \xi^{fwd}H\right) + 2v\frac{dG}{du}.$$
(Eq.43)

Substituting  $\varepsilon_f$  (Eq.9),  $\frac{dG}{du}$  (Eq.16),  $\xi^{fwd}$  (Eq.34),  $\frac{d\varepsilon_f}{du}$  (Eq.41), and  $\frac{d\xi^{fwd}}{du}$  (Eq.42) in  $\frac{dX}{du}$  (Eq.43) yields

$$\frac{dX}{du} = \frac{\left(\varepsilon_y \left(\frac{2c^2}{u^3} + \frac{2c^2v_y}{u^3}\right) + \frac{HA^*}{\rho q^M}\right)D^* + \frac{2v(G - X)}{u} + \frac{(E^A - E^M)C^*A^*}{\rho q^M}}{\frac{(E_A - E_M)C^*B^*}{\rho q^M} + \frac{HD^*B^*}{\rho q^M} + 1}$$
(Eq.44)

where

$$A^* = \frac{1}{2}\Delta S_{33}(\frac{4Gv(G-X)}{u} - \frac{4G(G-X)}{u} + \frac{4Xv(G-X)}{u} + \frac{H(G-X)}{u} + \frac{H(G-X)}{u})$$

$$B^* = H + \Delta S_{33}(X - 2Gv)$$

$$C^* = \varepsilon_y \left(v_y \left(\frac{c^2}{u^2} - 1\right) + \frac{c^2}{u^2}\right) + \frac{HE^*}{\rho q^M}$$

$$D^* = E^A + \frac{(E^A - E^M)E^*}{\rho q^M}$$

$$E^* = H(G-X) - \rho \Delta s_0 (T - M_s) - \rho \Delta b \left[ (T - T_0) - T ln \left(\frac{T}{T_0}\right) \right]$$

$$+ \frac{1}{2}\Delta S_{33}(2G^2v - 2G^2 - X^2 + 4XGv).$$

The updated expression for  $\frac{dX}{du}$  (Eq.44) is in terms of X, G, and u and with the governing radial equilibrium ODE (Eq.16), a system of nonlinear differential equations is formed with proper initial boundary conditions and can be solved numerically in Matlab using an explicit Runge-Kutta algorithm,

In heterogenous forward transformation and austenite, the boundary condition of the forward transformation is located at the transformation front where the forward martensitic volume fraction,  $\xi^{fwd}$ , is equal to zero. The axial stress, X, compressive stress, G, and filament length ratio, u, at the transformation front is solved at a given yarn strain,  $\varepsilon_y$ , from a system of equations containing (Eq.38), (Eq.39), and setting the forward martensitic volume fraction,  $\xi^{fwd}$  (Eq.34), equal to zero. The axial stress,

X, and compressive stress, G, at the transformation front are used as boundary conditions in the nonlinear system of equations,  $\frac{dG}{du}$  (Eq.16) &  $\frac{dX}{du}$  (Eq.44), and the stresses for the forward transformation section of the yarn are determined.

#### 6.3. Loading of homogeneous forward transformation

In this loading evolution (Figure 3), the forward transformation will continue to grow outward until the entire yarn is in a homogenous forward transformation state (Figure 3c). In homogenous forward transformation, the same system of nonlinear differential equations,  $\frac{dG}{du}$  (Eq.16) &  $\frac{dX}{du}$  (Eq.44), outlined in Sec. 6.2, is used to solve for the axial stress X, and compressive stress, G. In this case, the transformation front has stopped expanding and the boundary conditions for the system are stable on the surface of the yarn. At the surface (u = 1), there is no compressive stresses (G(1) = 0), and the axial stress X (Eq.40), and forward martensitic volume fraction  $\xi^{fwd}$  (Eq.34), is simplified and solved. The system of nonlinear differential equations,  $\frac{dG}{du}$  (Eq.16) &  $\frac{dX}{du}$  (Eq.44), is then solved to determine the stresses in the yarn. The forward martensite volume fraction,  $\xi^{fwd}$  (Eq. 34), is calculated for all elements to check for the completion of the forward transformation, or when  $\xi^{fwd}$  is greater than one

#### 6.4. Loading of heterogeneous forward transformation and SIM

The forward transformation reaches completion when the material has fully transformed into stressed induced martensite. This transition occurs when the forward martensitic volume fraction,  $\xi^{fwd}$ , is calculated (Eq.34) to be greater than one. When this occurs, the yarn is in a heterogeneous state of SIM and forward transformation (Figure 3d). The SIM will appear first in the yarn center, where the equivalent stress is highest (Eq.31) due to the elevated filament strain and increased compressional stresses. The boundary of the SIM will grow outward towards the surface of the yarn. The portion of the yarn remaining in forward transformation is solved according to Sec. 6.3 since the boundary condition remains on the surface of the yarn.

In SIM, the transformation function,  $\Phi$  (Eq.28), returns to the elastic domain and the forward martensitic volume fraction,  $\xi^{fwd}$ , is constant at one. The material is treated as a linear elastic isotropic material with a material modulus equal to,  $E^M$ , and the axial stress, X, is updated to

$$X = (\varepsilon_f - H) * E^M + 2G\nu.$$
 (Eq.45)

In SIM, the forward martensitic volume fraction,  $\xi^{fwd}$ , is not a function of filament length ratio, u, and the axial stress, X, is substituted in the governing radial equilibrium ODE (Eq.16) and solved for the compressive stress, G, with the proper boundary condition. In this scenario, the boundary of the SIM region is on the transformation front where the forward martensitic volume fraction (Eq. 33) equals exactly one ( $\xi^{fwd} = 1$ ). The compressive stress, G, and filament length ratio, u, at the boundary is numerically approximated, and the compressive stress, G, for the remaining SIM elements is solved from the ODE (Eq.16). Lastly, the compressive stresses are substituted back into (Eq.45) to solve for the axial stress, X.

## 6.5. Loading of homogeneous SIM

The SIM region will continue to grow outward until it reaches the surface of the yarn (Figure 3e), and the yarn is in a homogenous SIM state. In homogenous SIM, the boundary of the SIM region is stable on the

outside surface of the yarn where G = 0, and u = 1. With a constant boundary condition, a closed-form solution for compression is solved from the radial equilibrium ODE (Eq.16) and is defined as

$$\frac{G}{=\frac{E^{M}u^{2\nu-1}\left(Hu^{2}+c^{2}\varepsilon_{y}+\varepsilon_{y}v_{y}u^{2}+2Hvu^{2}-2c^{2}\varepsilon_{y}v+c^{2}\varepsilon_{y}v_{y}-2c^{2}\varepsilon_{y}vv_{y}+2\varepsilon_{y}vv_{y}u^{2}\right)}{u^{2\nu+1}(4v^{2}-1)}} - \frac{E^{M}u^{2\nu-1}\left(H+2Hv+\varepsilon_{y}v_{y}+c^{2}\varepsilon_{y}+2\varepsilon_{y}vv_{y}-2c^{2}\varepsilon_{y}v+c^{2}\varepsilon_{y}v_{y}-2c^{2}\varepsilon_{y}vv_{y}\right)}{4v^{2}-1}}{4v^{2}-1} (Eq.46)$$

The compressive stress is substituted back into (Eq.46) to solve for the axial stress, *X*. The yarn will remain in homogenous SIM until the completion of loading.

## 7. Material phase evolution during yarn unloading

A well-known advantage of using a superelastic material is the material's ability to recover large deformations upon unloading. While in a complex architecture, SMA microfilament yarns leverage this material characteristic to provide enhanced recoverable deformations. Unlike loading, in which the entirety of the yarn is assumed to be in an initial homogenous austenite state, unloading can occur from any stage in loading evolution (Figure 3). For this paper, we outline two unloading evolutions from a homogeneous SIM yarn (Figure 4) and a heterogeneous forward transformation and SIM yarn (Figure 5) since it is assumed that most unloading situations follow these paths. To identify the phases present in the yarn at the onset of unloading, the forward martensitic volume fractions at the end of loading are saved in the martensitic volume fraction at reversal,  $\xi^{t-r}$ , and are used guide the unloading solution procedure.

### 7.1. Unloading from homogeneous SIM

If the yarn unloads from homogeneous SIM, unloading follows a simple path that appears similar to the loading path in reverse (Figure 4f-j). During homogeneous SIM unloading (Figure 4f), the axial stress, X, and the compressive stress, G, are solved in the same way as in Sec. 6.5, using equations (Eq.45) and (Eq.46). The updated stresses are used to calculate the reverse martensitic volume fraction,  $\xi^{rev}$  (Eq.35), to check for the onset of reverse transformation, which occurs when the martensite volume fraction is less than one ( $\xi^{rev} < 1$ ).

Upon unloading, the reverse transformation will begin on the outside surface of the yarn where the equivalent stresses are the smallest, and the transformation front will grow inward towards the center of the yarn. The yarn will then be in a heterogeneous state of reverse transformation and SIM (Figure 4g). The portion in reverse transformation is solved using the nonlinear system of differential equations,  $\frac{dG}{du}$  (Eq.16) &  $\frac{dX}{du}$  (Eq.44), outlined in Sec. 6.3 but updated with the reverse martensitic volume fraction,  $\xi^{rev}$  (Eq.35). In this evolution stage, the boundary condition location is constant on the surface of the yarn. The remaining SIM portion is solved using the stresses at the transformation front as the initial condition for the SIM solution procedure outlined in Sec. 6.4. The reverse transformation front will continue to grow inward towards the center of the yarn until the yarn is in a homogeneous reverse transformation state (Figure 4h).

After each unloading step, the reverse martensitic volume fraction,  $\xi^{rev}$  (Eq.35), is calculated to check for the completion of the reverse transformation, which occurs when the reverse martensitic volume fraction is equal to or less than zero. The completion of the reverse transformation indicates that a portion of the

yarn has returned to an austenitic state, and the yarn is in a heterogeneous state of austenite and reverse transformation (Figure 4i). The portion of the yarn in austenite is solved first according to the procedure outlined in Sec. 6.1 with the initial condition on the outside surface of the yarn.

The transformation front at the end of the austenite portion, where  $\xi^{rev} = 0$ , is used to solve for the boundary conditions of the remaining reverse transformation. The stresses of the remaining reverse transformation elements are then solved using the procedure outlined in Sec. 6.2, but updated with the reverse martensitic volume fraction,  $\xi^{rev}$  (Eq.35). Upon further loading, the yarn will be in a homogenous austenite state and unload back to the initial state at the onset of loading.

#### 7.2. Unloading from heterogeneous forward transformation and SIM

The yarn geometry (filament diameter, twist, number of filaments, packing density, etc.) influences the distribution of stresses and strains in the yarn at the end of loading. Consequently, there are many possible yarn unloading evolutions from a state of heterogeneous forward transformation and SIM. However, for this paper, we will detail a single pathway (Figure 5) that can be generalized for other unloading evolutions.

If any portion of the yarn is in forward transformation at the conclusion of loading, the yarn unloads from a heterogeneous state of incomplete forward transformation and SIM (Figure 5f). The unloading procedure for the incomplete forward transformation portion is altered due to the inclusion of the martensitic volume fraction at reversal,  $\xi^{t-r}$ . The effective material properties of such yarn elements are defined by a rule of mixtures (Eq.20); specifically, the material modulus is defined as

$$E = E^{A} + \xi^{t-r} (E^{M} - E^{A}).$$
 (Eq.47)

The axial stress equation is updated to

$$X = \left(\varepsilon_f - \xi^{t-r}H\right) * E + 2G\nu, \tag{Eq.48}$$

where the martensitic volume fraction at reversal,  $\xi^{t-r}$ , is treated as a function of filament length ratio, u, by polynomial fitting the martensitic volume fractions at the onset of unloading for elements with incomplete forward transformations. To calculate the unloading stresses of the incomplete forward transformation portion of the yarn, the axial stress, X (Eq.48), is used in the governing ODE (Eq.16) and solved with the initial condition on the surface of the yarn. The boundary of the remaining SIM section is numerically approximated by solving when the martensitic volume fraction at reversal is equal to one, and the SIM elements are solved according to Sec. 6.4.

The updated stresses are then used to calculate the reverse martensitic volume fraction to check for the onset of reverse transformation. The elements unloading from forward transformation will begin reverse transformation when the reverse martensitic volume fraction,  $\xi^{rev}$ , is below the martensitic volume fraction at reversal,  $\xi^{t-r}$ . Meanwhile, the elements unloading in SIM will begin reverse transformation when the reverse martensitic volume fraction,  $\xi^{rev}$ , is below one. Consequently, the reverse transformation onset conditions are dissimilar at different radial positions, and it is not guaranteed that reverse transformation will begin on the surface of the yarn. For this exercise, we will outline a case in which reverse transformation initiates on the surface of the yarn, and the transformation front grows inward towards the center of the yarn. The general solution procedure could be expanded for the case where reverse transformation begins inside the yarn.

When reverse transformation has started, it is possible for the yarn to be in a heterogeneous state of reverse transformation, incomplete forward transformation, and SIM (Figure 5g). The solution procedure starts with the outermost portion, where the initial condition is on the surface of the yarn and works inward using the updated stresses to approximate the initial conditions of the next distinct region. In this scenario (Figure 5g), the outermost reverse transformation is solved using the updated version of the nonlinear system of equations,  $\frac{dG}{du}$  (Eq.16) &  $\frac{dX}{du}$  (Eq.44), followed by unloading from forward transformation, which is solved using the axial stress, X (Eq.48), and governing ODE (Eq.16). Lastly, the remaining SIM portion is solved according to Sec. 6.4.

Upon further unloading, the reverse transformation will continue to grow inward until the yarn is in a heterogeneous state of reverse transformation and SIM (Figure 5h). Eventually, elements in the yarn will complete the reverse transformation to austenite when the reverse martensite volume fraction,  $\xi^{rev}$ , is less than zero. Similar to reverse transformation, this is not guaranteed to initiate on the surface of the yarn, although it does occur in this unloading evolution. When austenite is present, the yarn will be in a heterogeneous state of austenite and reverse transformation (Figure 5i). The austenite front grows inward towards the center of the yarn until the yarn is in a homogeneous austenite state (Figure 5j) until the completion of unloading (solution procedure in Sec. 7.1). The yarn has finished unloading back to the initial state, and the microfilament and macroscopic yarn responses are analyzed.

## 8. Modeling Results

The microfilament response is dependent on yarn parameters (filament diameter, number of filaments, twist) and loading conditions (temperature, yarn displacement); however, a general pattern of behavior can be identified from a single configuration. To discuss the patterns observed in the microfilament response, we modeled a 6.32 twist per centimeter (TPCM) yarn consisting of 400 microfilaments of 10  $\mu$ m diameters subjected to a displacement of 15.0% structural strain. The model predicts the spatially distributed axial filament stress, X, tangential filament stress, G, and phase evolution on the mesoscale during loading and unloading (Figure 6). The contribution of all filaments is summed to predict the macroscopic yarn force.

## 8.1. Meso- to microscopic loading of yarn element

During initial loading from 0 to 0.84% structural strain, at a temperature above austenite finish, all filaments in the yarn structure exhibit linearly increasing axial filament stress (Figure 6a). All filaments, except the outer surface filaments, exhibit linearly decreasing tangential filament compression (Figure 6b). Due to the spatially distributed filament strain from rigid body radial contraction, the modulus of the axial stress (Figure 6a) is at a maximum of (64.4GPa) at the center filament (black), and at a minimum of (42.8GPa) on the surface of the yarn (green). Additionally, the tangential compression modulus (Figure 6b) is at a maximum absolute value (8.56GPa) on the center filament (black) and equal to zero on the surface filament (green) due to the governing radial equilibrium ODE boundary condition. The onset of forward transformation occurs at 0.84% structural strain in the center of the yarn, where the equivalent von Mises stress (Eq.31) is highest.

During SMA forward transformation, mechanical energy is dissipated as thermal energy during the solid-state phase transition from austenite to stressed induced martensite, resulting in a stress plateau. In a yarn with a heterogeneous state of forward transformation and austenite (from 0.84% to 1.43% structural strain), the non-constant transformation front boundary condition forces the tangential filament

compression (Figure 6b) to decrease nonlinearly (black). To maintain the stress plateau in the equivalent stress, the axial stress (Figure 6a) compensates by nonlinearly decreasing (black).

Heterogeneous forward transformation ends when the yarn surface filament reaches forward transformation (1.43% structural strain). During homogeneous forward transformation (1.43% to 8.38% structural strain), the transformation front boundary condition stabilizes on the surface of the yarn, and the nonlinear compensation that was present in heterogeneous forward transformation and austenite ceases. The axial stress and tangential compression of the surface (green) and center (black) filaments continue in a stress plateau (Figure 6).

The center filaments (black) will be the first to finish forward transformation and enter SIM (8.38% structural strain). At this strain, the yarn will be in a heterogeneous state of forward transformation and SIM. The transformation front grows outward towards the surface of the yarn, forcing a non-constant boundary for the SIM portion. In SIM, the SMA material has returned to the elastic regime (Eq.28) and loads linearly in the von Mises equivalent stress. However, for the elements in SIM, the changing boundary condition forces the tangential compression (Figure 6b) of the center filaments (black) to decrease nonlinearly. While subtle, the axial stress (Figure 6a) of the center filament (black) also compensates nonlinearly to maintain elastic loading in the von Mises equivalent stress.

Filaments in the center (black) are in forward transformation for a total of 7.54% structural strain from 0.84% to 8.38% structural strain (Figure 6), which is comparable to values seen in monofilament SMA [49]. However, the surface filaments (green) have an extended forward transformation structural strain range of 12.5% from 1.43% to 13.9% structural strain, a 65.4% increase over the center filaments. This increased forward transformation range is due to the spatially distributed filament strain,  $\varepsilon_f$ , from the increased radial contraction in the outer surface filaments.

In this loading evolution, the surface filament (green) completes the forward transformation at 13.9% structural strain, and the yarn enters a state of homogeneous SIM. The axial stress (Figure 6a) increases linearly, and the tangential compression (Figure 6b) decreases linearly until the completion of loading. In homogeneous SIM, the axial stress of the center filament (black) loads with a maximum linear modulus of 23.0GPa while the surface filament (green) loads with a minimum linear modulus of 15.3GPa. The tangential compression of the center filament (black) loads with a maximum modulus absolute value of 3.05GPa compared to zero for the surface filament (green).

## 8.2. Meso- to microscopic unloading of yarn element

If homogeneous SIM is reached, the axial stress (Figure 6a) and tangential compression (Figure 6b) in all filaments will load linearly with the same modulus but in the opposite direction as they did during homogeneous SIM loading. The linear loading will continue until the outer surface of the yarn begins reverse transformation at a stress and strain that is lower than that for forward transformation (11.0% structural strain).

The yarn will then be in a heterogeneous state of reverse transformation and SIM (11.0% to 6.67% structural strain), with the reverse transformation front growing inward towards the center of the yarn. The elements in reverse transformation have a stable boundary condition on the outside of the yarn, and the axial stress (Figure 6a) and tangential compression (Figure 6b) for the surface filament (green) undergo constant stress plateaus. The remaining filaments in SIM, including the center filament (black), have a non-constant boundary from the inwardly growing reverse transformation front. Consequently, the tangential compression (Figure 6b) increases nonlinearly, and the axial stress (Figure 6a) compensates to maintain elastic behavior in the equivalent von Mises stress.

Upon further unloading (6.67% to 0.39% structural strain), the yarn will be in homogeneous reverse transformation. All the filaments will be in a constant stress plateau, with the boundary condition stable on the surface of the yarn. The surface filament (green) will first complete the reverse transformation to austenite (0.39% structural strain), and the yarn will be in a state of heterogeneous austenite and reverse transformation (0.39% to 0.23% structural strain).

The austenite portion will unload linearly with the same modulus seen in loading. The remaining reverse transformation, including the center filament (black), will nonlinearly adapt to the changing boundary condition at the end of the austenitic region to maintain a stress plateau in the equivalent von Mises stress. Eventually, the yarn will be in homogeneous austenite and will unload back to the initial state with the same modulus seen in loading.

#### 8.3. Meso- to macroscopic behavior

Microfilament behavior heavily contributes to global yarn behavior. The axial tension and tangential compression on each radial element contribute a force, f (Eq.17), to the global yarn force, F (Eq.18). The elemental force contributions are summated over the entire yarn to calculate the yarn force, F, for any given yarn strain (Figure 6c). In homogeneous austenite loading (0% to 1.43% structural strain), the individual filament moduli summate to create an effective yarn modulus of 44.56GPa (Figure 6c). The effective yarn modulus is normalized to the cross-sectional area of the active material in the untwisted yarn. Higher twisted yarn configurations have a broader distribution of filament moduli, resulting in a lower effective yarn modulus. For homogeneous states, such as homogeneous austenite, the yarn exhibits stable, linear behavior. However, when the yarn is in a heterogeneous state, multiple phases within the varn contribute to the nonlinear transition regions seen in the global force behavior. The lengths of the nonlinear transition regions are defined by the length of the heterogeneous states of the yarn, which are influenced by the distribution of strains across the radial elements. At lower structural strains, the distribution of strains is more compact (Eq.9), and the nonlinear transitions are shorter. For example, the duration of the transition from austenite to forward transformation is 0.59% structural strain, compared with 5.52% for the transition between forward transformation and SIM (Figure 6c). Higher twisted yarn configurations have more distributed stress and strains, resulting in extended nonlinear heterogeneous states of the yarn. Overall, the nonlinear transitions enable the yarn structure to handle higher maximum elongations and, during unloading, recover significant structural strains.

#### 9. Model Validation

The microfilaments were created by Fort Wayne Metals using an accumulative drawing/rolling and bonding technique. The NiTi alloy used in this study has a chemical composition of 56wt% nickel with 300ppm oxygen, 310ppm carbon, and balanced titanium. It is a nickel-rich material, with an ingot A<sub>f</sub> of 68°C. Each microfilament bundle consists of 400 microfilaments with 10 $\mu$ m diameters. The bundles were processed into yarns in an industrial ring spinner at a local fiber processing and yarn spinning mill. Manufacturing spindle speed and delivery speed were controlled to manage the amount of twist inserted into the yarns. Five distinct yarn configurations were made with different manufacturing twists ranging from 0.70 TPCM to 10.54 TPCM. To shape-set the yarn structure, each yarn was thermally processed in a custom-built in-line reel to reel system that travels through a tube furnace at 500°C for 120 seconds under a set tension after twist insertion (Figure S1b, Supporting Information). The tension during thermal processing was adjusted for the level of twist in the yarns. Higher twisted yarns needed higher tensions during processing to remove the increased manufacturing strains and twist set the structure. To validate the model, a variety of material, geometric, and mechanical tests were conducted. Differential scanning

calorimetry (DSC) was performed to determine the transformation temperatures of the microfilaments (Figure S1a & Table 1). SEM and microscopy imaging were performed to identify the packing density,  $\varphi$ , used for all yarn configurations (Figure S2b & Table 1). A series of isothermal experiments were performed on the five yarn configurations on an RSA-G2 dynamic mechanical analyzer (DMA) with an environmental chamber for temperature control. Displacement controlled tests were performed at a macroscopic strain rate of  $\dot{\delta}L^{-1} = \pm 5 \times 10^{-5} \, s^{-1}$  and at a temperature of 80°C, well above austenite finish temperature,  $A_f$ . DMA tests were performed on a 0.70TPCM yarn to identify the austenite modulus,  $E^A$ , martensitic modulus,  $E^M$ , model parameter,  $\rho\Delta s_0$ , and the maximum uniaxial transformation strain, H, that are used for all yarn configurations (Table 1). After calibration, the model was run for the five yarn configurations and compared to the experimental curves (Figure 7).

During initial loading, the model predicts the inverse relationship between increasing twist and decreasing effective yarn modulus. Experimental results demonstrated a 84.9% decrease from a homogeneous austenite effective yarn modulus of 71.0GPa in the 0.70TPCM yarn to 10.7GPa in the 10.54TPCM yarn (Figure 7a). Meanwhile, the model captured a 67.1% decrease in effective yarn modulus from 69.5GPa in the 0.70TPCM yarn to 22.89GPa in the 10.54TPCM yarn (Figure 7b). At higher twists, there is more variation in filament axial strain (Eq.9) within the yarn structure, resulting in a wider range of stresses and a decrease in effective yarn modulus, which is captured in both experimental and modeling results (Figure 7b).

The homogeneous austenite effective modulus ends with the onset of forward transformation and a nonlinear transition (heterogeneous state) to homogeneous forward transformation. It is observed in experimental results (Figure 7a) that the forces and lengths of the nonlinear transitions are impacted by the twist. The 0.70TPCM yarn exhibits a short transition of 0.74% structural strain from 15.28N to 19.53N force. However, the 10.54TPCM yarn transitions over an extended range of 3.02% structural strain at significantly lower forces of 6.05N to 11.0N (Figure 7a). The model captures this pattern of behavior: the 0.70TPCM yarn transitions almost instantaneously in 0.01% structural strain at 18.98N to 19.13N while the 10.54TPCM yarn transitions over a range of 2.53% structural strain from 6.47N to 10.77N (Figure 7b). The impact of twist on the nonlinear transitions is explained by a couple of factors. First, the length of the nonlinear transitions is bounded by the length of the heterogeneous states, which are longer when the distribution of strain is broader for higher twists and at higher structural strains. Secondly, the forces at which these nonlinear transitions occur are influenced by the impact twist has on compressional stresses in the yarn. Higher twisted yarns have larger compressional stresses and lower axial stresses (Eq.38). While both axial stress and tangential compression contribute to the equivalent von Mises stress, axial stress contributes more to the total yarn force, F, than tangential compression due to geometric constants described in (Eq.18). As a result, higher twisted yarns experience nonlinear transitions at lower forces than lower twisted configurations. The same explanations can be applied to the lower forces and expanded transition lengths observed in the higher twisted experimental yarns throughout the remaining loading and unloading (Figure 7a).

The loading evolution can end in multiple yarn states, which impact the unloading behavior. If the yarn reaches homogeneous SIM by the end of loading, then unloading will occur with the same localized effective modulus as SIM, as shown in the modeling results in the 0.70TPCM and 3.51TPCM yarns (Figure 7b). However, if the yarn is in a heterogeneous state of forward transformation and SIM at the completion of loading, then the effective unloading modulus will differ from the loading modulus. The variation in effective loading and unloading moduli is visible in the 5.27, 7.03, and 10.54TPCM yarns in Figure 7b. At the end of loading of the modeled 5.27TPCM yarn, the localized effective modulus was estimated to be 14.5GPa. Because 23.3% of the filaments remained in forward transformation, the

effective unloading modulus was predicted to be 18.4GPa for a 26.7% change in modulus. While the exact percentage of filaments in forward transformation at the end of loading can not be derived from the experimental curves (Figure 7a), a similar pattern of moduli changes is observed, indicating a heterogeneous mixture of phases is present in the yarn at the end of loading. Unlike the model results, the 0.70 and 3.51TPCM yarns do not exhibit the same effective loading and unloading moduli. This is attributed to two factors; the first is a change in frictional forces from the reversal of loading direction that is currently neglected in the model. Secondly, it is hypothesized that the change in loading direction could cause a change in the yarn contraction ratio,  $v_y$ , which is currently modeled as constant. Like the modeling results, the higher twisted 5.27, 7.03, and 10.54TPCM experimental yarns demonstrate an exaggerated change in modulus from loading to unloading (Figure 7a). At the end of loading, the 10.54TPCM yarn has a localized effective modulus of 2.88GPa compared to a modulus of 28.3GPa at the start of unloading, an order of magnitude change in modulus from the presence of forward transformation remaining in the yarn.

To validate the model's ability to capture unloading from unique yarn phase evolution stages, 3.51 TPCM yarns were loaded to various increasing structural strains and unloaded (Figure 7c). While the exact phase evolution stage is unknown in the experimental data, it is observed that with increasing structural strain, the effective yarn unloading modulus decreases. This is because the effective material moduli, E, of the filaments in forward transformation will be transitioning from their original austenitic modulus,  $E^A$ , to the decreased martensitic modulus,  $E^M$ , at the end of forward transformation (rule of mixtures, (Eq.20). Increased structural straining correlates to a higher percentage of filaments that have either started, completed, or are farther along in the forward transformation, resulting in a decreased effective yarn modulus exhibited during unloading. Experimentally, this is observed in the 41.1% decrease in the effective yarn modulus from unloading at 2.5% structural strain compared with unloading at 10.0% structural strain (Figure 7c).

The experimental data was compared with model simulations of identical loading scenarios of a 3.51 TPCM yarn (Figure 7d). The model was able to capture the decrease in effective yarn unloading modulus as a result of a higher percentage of the filaments in forward transformation quantifiable by the mean filament value of forward martensitic volume fraction of the filaments. At 2.5% structural strain, all the filaments are in forward transformation, however the mean forward martensitic volume fraction of 0.22 implies that the filaments are early along in their transformation (completion at  $\xi^{fwd} = 1$ ). At 5.0%, 7,5% and 10.0% structural strain, the mean martensitic volume fractions were 0.55, 0.84, and 1.0. At higher structural strains, the filaments were further along in the forward transformation, resulting in a 58.4% decrease in the effective yarn unloading modulus from the 2.5% structural strain loading to the 10.0% structural strain loading, similar to the 41.1% decrease observed experimentally (Figure 7c).

While the model qualitatively predicts the impact of the twist on the effective modulus, transition regions, unloading behavior, and forces, there is room for improvement. Qualitatively, it is observed in the experimental data that the transformation slopes increase with increasing yarn twist while the model predicts pseudoelastic force plateaus for all yarn configurations. Quantitatively, it is observed from error analysis (Figure 8), where the error is defined as the percent relative difference between the experimental force and modeling force, that the model struggles to quantitatively predict the forces at the beginning and end of loading and unloading. Percent relative difference peaks, up to a maximum of 78.7% in the 7.03TPCM yarn, are observed during the initial loading period (0% to ~2% structural strain). The model does align with the experimental data, as the percent relative difference quickly decreases below 25% at ~2.00% structural strain and sustains lower percent relative differences for the remainder of loading. During unloading, the percent relative difference in the 7.03TPCM yarn stays consistently below 40%

(~12% to 4% structural strain) until peaking again to 99.0% at the end of unloading (~2% structural strain). The high percent relative difference observed in unloading is attributed to permanent deformation sustained by some filaments in loading and is not accounted for in the model.

The differences between the model and experimental results are hypothesized to result from multiple considerations not currently accounted for in the model, such as permanent deformation, manufacturing inconsistencies, frictional forces, and non-constant contraction ratio. The non-constant contraction ratio is hypothesized to have the most significant impact on the accuracy of the model. An earlier assumption stated that the yarn contraction ratio,  $v_y$ , is a constant; however, this is an assumption made for linear elastic materials. The yarn contraction ratio plays a large role in the variation of filament strain, and thus the filament stresses within the yarn at any given structural strain. Accounting for a non-constant contraction ratio could improve the predictive ability of the model by distributing the filament strains more broadly. More variation in filament strain would result in decreased effective moduli, decreased transition forces, increased transition lengths, and increased phase heterogeneity, all of which would improve the predictive capability of the model. Additionally, increased and non-constant contraction could lead to exaggerated filament interlocking and enlarged frictional forces, resulting in the structural hardening behavior observed in the increasing transformation slopes of higher twisted yarns. Understanding the change in contraction ratio during phase transformations could be critical for capturing the shape of the experimental yarns after initial loading, therefore improving the overall accuracy.

#### 10. Conclusion

In this paper, we develop a predictive model for the superelastic behavior of SMA microfilament yarns by modifying existing structural and material models to interoperate. The semi-analytical model uses a hierarchical approach to provide insight into the microfilament response to predict and explain the macroscale behavior of the yarn. Linear elastic based yarn models are redefined with 3D phenomenological SMA constitutive equations. During yarn loading and unloading, the material phases present in the yarn are identified using a martensitic volume fraction, and the appropriate stress equations are applied. Common loading and unloading evolutions are outlined in the context of the microfilament kinematics to map to the macroscopic yarn force response. To validate the model, the yarn force response is compared with experimental data for five yarns with varying twists. The model is shown to accurately predict relationships between the yarn response and twist, including effective loading modulus and exaggerated transition regions between phases through an understanding of the microfilament response. Lastly, the addition of a non-constant contraction ratio is discussed to offer improvements over the quantitative accuracy of the model.

The semi-analytical model fills a knowledge gap necessary for the functionalized integration of SMA microfilament yarns. Using the model, manufacturing decisions can be made to produce SMA microfilament yarns with desired mechanical characteristics, such as effective modulus, for specific application needs. Insight in the microfilament stress and strains provides designers with safe application strains to avoid failure or significant permanent deformations. Additionally, the microfilament strains can provide insight into the consistent cycled behavior, which is influenced by the extent of the material straining. This model establishes a foundation for creating a predictive model for the actuation behavior of SMA yarns that use the shape memory effect. For other multifunctional material systems, this model provides a framework for working within the complex yarn architecture. Lastly, this paper institutes a mechanical understanding of SMA yarn behavior that can be implemented within existing textile models to predict the performance of functionalized cloth-like multifunctional SMA textiles for wearable, robotic, medical, defense, and transportation applications.

## 11. Supporting Information

Supporting Information is available from the journal or the author.

## 12. Acknowledgments

This work was supported by an NSF CAREER Award Grant and an Industrial Partnership Grant from Minnesota's Discovery, Research, and InnoVation Economy Robotics, Sensors, and Advanced Manufacturing (MnDRIVE RSAM) Initiative with Fort Wayne Metals. We thank Prof. Mohammad Elahinia for discussions regarding his solution procedure, Polymer Characterization Facility at the University of Minnesota for the use of their DMA and DSC, Paul Sims and Tom Hamilton at Fort Wayne Metals for their help on developing NiTi microfilaments, Matt Zumbrum for solution discussions, Kevin Eschen for modeling discussions, Rachael Granberry for yarn and figure discussions, and the rest of the Design of Active Materials and Structures Laboratory for their support.

#### 13. References

- [1] Zhao Z, Yan C, Liu Z, et al. Machine-Washable Textile Triboelectric Nanogenerators for Effective Human Respiratory Monitoring through Loom Weaving of Metallic Yarns. Advanced Materials 28:10267–10274. https://doi.org/10.1002/adma.201603679
- [2] Lee JA, Aliev AE, Bykova JS, et al. (2016) Woven-Yarn Thermoelectric Textiles. Adv Mater 28:5038–5044. https://doi.org/10.1002/adma.201600709
- [3] Soin N, H. Shah T, C. Anand S, et al. (2014) Novel "3-D spacer" all fibre piezoelectric textiles for energy harvesting applications. Energy & Environmental Science 7:1670–1679. https://doi.org/10.1039/C3EE43987A
- [4] Lee J-H, Chung YS, Rodrigue H (2019) Long Shape Memory Alloy Tendon-based Soft Robotic Actuators and Implementation as a Soft Gripper. Scientific Reports 9:11251. <a href="https://doi.org/10.1038/s41598-019-47794-1">https://doi.org/10.1038/s41598-019-47794-1</a>
- [5] Veeramani AS, Buckner GD, Owen SB, et al. (2008) Modeling the dynamic behavior of a shape memory alloy actuated catheter. Smart Mater Struct 17:015037. https://doi.org/10.1088/0964-1726/17/01/015037
- [6] Wischke C, Neffe AT, Steuer S, Lendlein A (2009) Evaluation of a degradable shape-memory polymer network as matrix for controlled drug release. Journal of Controlled Release 138:243–250. <a href="https://doi.org/10.1016/j.jconrel.2009.05.027">https://doi.org/10.1016/j.jconrel.2009.05.027</a>
- [7] Ula SW, Traugutt NA, Volpe RH, et al. (2018) Liquid crystal elastomers: an introduction and review of emerging technologies. Liquid Crystals Reviews 6:78–107. <a href="https://doi.org/10.1080/21680396.2018.1530155">https://doi.org/10.1080/21680396.2018.1530155</a>
- [8] Shen C, Wu Z, Gao Z, et al. (2017) Impact protection behavior of NiTi shape memory alloy wires. Materials Science and Engineering: A 700:132–139. <a href="https://doi.org/10.1016/j.msea.2017.05.097">https://doi.org/10.1016/j.msea.2017.05.097</a>
- [9] Benafan O, Moholt MR, Bass M, et al. (2019) Recent Advancements in Rotary Shape Memory Alloy Actuators for Aeronautics. Shap Mem Superelasticity 5:415–428. https://doi.org/10.1007/s40830-019-00260-3
- [10] Reedlunn B, Daly S, Shaw J (2013) Superelastic shape memory alloy cables: Part I Isothermal tension experiments. International Journal of Solids and Structures 50:3009–3026. https://doi.org/10.1016/j.ijsolstr.2013.03.013
- [11] Reedlunn B, Daly S, Shaw J (2013) Superelastic shape memory alloy cables: Part II Subcomponent isothermal responses. International Journal of Solids and Structures 50:3027–3044. https://doi.org/10.1016/j.ijsolstr.2013.03.015
- [12] Kianzad S (2015) A treatise on highly twisted artificial muscle: thermally driven shape memory alloy yarn and coiled nylon actuators. University of British Columbia
- [13] Granberry, R., Berry, J., Holschuh, B., Abel, J., "Kinetically Tunable, Active Auxetic, and Variable Recruitment Smart Textiles from Hierarchical Assemblies" *Under Review*
- [14] Weinberg CA, Cai S, Schaffer J, Abel J Multifunctional Spun Yarns and Textiles from Nickel-Titanium Microfilaments. Advanced Materials Technologies n/a:1901146. https://doi.org/10.1002/admt.201901146
- [15] J. W. S. Hearle, P. Grosberg, S. Backer, Structural Mechanics of Fibers, Yarns, and Fabrics. 19690000, 1.
- [16] Kim SH, Haines CS, Li N, et al. (2017) Harvesting electrical energy from carbon nanotube yarn twist. Science 357:773–778. https://doi.org/10.1126/science.aam8771
- [17] Dong K, Deng J, Ding W, et al. (2018) Versatile Core-Sheath Yarn for Sustainable Biomechanical Energy Harvesting and Real-Time Human-Interactive Sensing. Adv Energy Mater 8:1801114. <a href="https://doi.org/10.1002/aenm.201801114">https://doi.org/10.1002/aenm.201801114</a>
- [18] Mu J, Andrade MJ de, Fang S, et al. (2019) Sheath-run artificial muscles. Science 365:150–155. https://doi.org/10.1126/science.aaw2403
- [19] Di J, Fang S, Moura FA, et al. (2016) Strong, Twist-Stable Carbon Nanotube Yarns and Muscles by Tension Annealing at Extreme Temperatures. Adv Mater 28:6598–6605. <a href="https://doi.org/10.1002/adma.201600628">https://doi.org/10.1002/adma.201600628</a>
- [20] Treloar LRG, Riding G (1963) 16—a Theory of the Stress-Strain Properties of Continuous-Filament Yarns. Journal of the Textile Institute Transactions 54:T156–T170. <a href="https://doi.org/10.1080/19447026308660166">https://doi.org/10.1080/19447026308660166</a>

- [21] Komori T (2001) A Generalized Micromechanics of Continuous-Filament Yarns. Part I: Underlying Formalism. Textile Research Journal 71:898–904. https://doi.org/10.1177/004051750107101008
- [22] Van Langenhove L (1997) Simulating the Mechanical Properties of a Yarn Based on the Properties and Arrangement of its Fibers Part I: The Finite Element Model. Textile Research Journal 67:263–268. https://doi.org/10.1177/004051759706700405
- [23] Sriprateep K, Bohez EL (2017) CAD/CAE for stress-strain properties of multifilament twisted yarns. Textile Research Journal 87:657–668. https://doi.org/10.1177/0040517516636000
- [24] Hearle JWS (1958) 29—THE MECHANICS OF TWISTED YARNS: THE INFLUENCE OF TRANSVERSE FORCES ON TENSILE BEHAVIOUR. Journal of the Textile Institute Transactions 49:T389–T408. https://doi.org/10.1080/19447025808662449
- [25] Treloar LRG (1962) Rubber models of yarns and cords: continuum theory. Br J Appl Phys 13:314–322. https://doi.org/10.1088/0508-3443/13/7/304
- [26] Khandelwal A, Buravalla V (2009) Models for Shape Memory Alloy Behavior: An overview of modeling approaches. International Journal of Structural Changes in Solids 38
- [27] Cisse C, Zaki W, Zineb TB (2016) A review of modeling techniques for advanced effects in shape memory alloy behavior. Smart Mater Struct 25:103001. https://doi.org/10.1088/0964-1726/25/10/103001
- [28] Paiva A, Savi MA (2006) An overview of constitutive models for shape memory alloys. In: Mathematical Problems in Engineering. https://www.hindawi.com/journals/mpe/2006/056876/. Accessed 8 Jan 2021
- [29] Patoor E, Lagoudas DC, Entchev PB, et al (2006) Shape memory alloys, Part I: General properties and modeling of single crystals. Mechanics of Materials 38:391–429. https://doi.org/10.1016/j.mechmat.2005.05.027
- [30] Birman V (1997) Review of Mechanics of Shape Memory Alloy Structures. Applied Mechanics Reviews 50:629–645. https://doi.org/10.1115/1.3101674
- [31] Mehrabi R, Kadkhodaei M, Elahinia M (2014) Constitutive modeling of tension-torsion coupling and tension-compression asymmetry in NiTi shape memory alloys. Smart Mater Struct 23:075021. https://doi.org/10.1088/0964-1726/23/7/075021
- [32] Brocca M, Brinson LC, Bažant ZP (2002) Three-dimensional constitutive model for shape memory alloys based on microplane model. Journal of the Mechanics and Physics of Solids 50:1051–1077. https://doi.org/10.1016/S0022-5096(01)00112-0
- [33] Brinson LC (1993) One-Dimensional Constitutive Behavior of Shape Memory Alloys: Thermomechanical Derivation with Non-Constant Material Functions and Redefined Martensite Internal Variable. Journal of Intelligent Material Systems and Structures 4:229–242. https://doi.org/10.1177/1045389X9300400213
- [34] Arghavani J, Auricchio F, Naghdabadi R, et al. (2010) A 3-D phenomenological constitutive model for shape memory alloys under multi-axial loadings. International Journal of Plasticity 26:976–991. https://doi.org/10.1016/j.ijplas.2009.12.003
- [35] Saleeb AF, Padula SA, Kumar A (2011) A multi-axial, multimechanism based constitutive model for the comprehensive representation of the evolutionary response of SMAs under general thermomechanical loading conditions. International Journal of Plasticity 27:655–687. <a href="https://doi.org/10.1016/j.ijplas.2010.08.012">https://doi.org/10.1016/j.ijplas.2010.08.012</a>
- [36] Tanaka K, Kobayashi S, Sato Y (1986) Thermomechanics of transformation pseudoelasticity and shape memory effect in alloys. International Journal of Plasticity 2:59–72. <a href="https://doi.org/10.1016/0749-6419(86)90016-1">https://doi.org/10.1016/0749-6419(86)90016-1</a>
- [37] Auricchio F, Taylor RL, Lubliner J (1997) Shape-memory alloys: macromodelling and numerical simulations of the superelastic behavior. Computer Methods in Applied Mechanics and Engineering 146:281–312. <a href="https://doi.org/10.1016/S0045-7825(96)01232-7">https://doi.org/10.1016/S0045-7825(96)01232-7</a>
- [38] Toi Y, Lee J-B, Taya M (2004) Finite element analysis of superelastic, large deformation behavior of shape memory alloy helical springs. Computers & Structures 82:1685–1693. <a href="https://doi.org/10.1016/j.compstruc.2004.03.025">https://doi.org/10.1016/j.compstruc.2004.03.025</a>

- [39] Toi Y, Choi D (2008) Computational Modeling of Superelastic Behaviors of Shape Memory Alloy Devices Under Combined Stresses. JCST 2:535–546. https://doi.org/10.1299/jcst.2.535
- [40] Mirzaeifar R, DesRoches R, Yavari A (2011) A combined analytical, numerical, and experimental study of shapememory-alloy helical springs. International Journal of Solids and Structures 48:611–624. <a href="https://doi.org/10.1016/j.ijsolstr.2010.10.026">https://doi.org/10.1016/j.ijsolstr.2010.10.026</a>
- [41] Mirzaeifar R, DesRoches R, Yavari A (2010) Exact solutions for pure torsion of shape memory alloy circular bars. Mechanics of Materials 42:797–806. https://doi.org/10.1016/j.mechmat.2010.06.003
- [42] Taheri Andani M, Alipour A, Eshghinejad A, Elahinia M (2013) Modifying the torque–angle behavior of rotary shape memory alloy actuators through axial loading: A semi-analytical study of combined tension–torsion behavior. Journal of Intelligent Material Systems and Structures 24:1524–1535. <a href="https://doi.org/10.1177/1045389X12474356">https://doi.org/10.1177/1045389X12474356</a>
- [43] Chapman C, Eshghinejad A, Elahinia M (2011) Torsional Behavior of NiTi Wires and Tubes: Modeling and Experimentation. Journal of Intelligent Material Systems and Structures 22:1239–1248. https://doi.org/10.1177/1045389X11411224
- [44] Boyd JG, Lagoudas DC (1996) A thermodynamical constitutive model for shape memory materials. Part I. The monolithic shape memory alloy. International Journal of Plasticity 12:805–842. <a href="https://doi.org/10.1016/S0749-6419(96)00030-7">https://doi.org/10.1016/S0749-6419(96)00030-7</a>
- [45] Qidwai MA, Lagoudas DC (2000) On thermomechanics and transformation surfaces of polycrystalline NiTi shape memory alloy material. International Journal of Plasticity 16:1309–1343. <a href="https://doi.org/10.1016/S0749-6419(00)00012-7">https://doi.org/10.1016/S0749-6419(00)00012-7</a>
- [46] Andani MT, Elahinia M (2014) A rate dependent tension—torsion constitutive model for superelastic nitinol under non-proportional loading; a departure from von Mises equivalency. Smart Mater Struct 23:015012. https://doi.org/10.1088/0964-1726/23/1/015012
- [47] Lagoudas D, Hartl D, Chemisky Y, et al (2012) Constitutive model for the numerical analysis of phase transformation in polycrystalline shape memory alloys. International Journal of Plasticity 32–33:155–183. https://doi.org/10.1016/j.ijplas.2011.10.009
- [48] Qidwai MA, Lagoudas DC (2000) On thermomechanics and transformation surfaces of polycrystalline NiTi shape memory alloy material. International Journal of Plasticity 16:1309–1343. <a href="https://doi.org/10.1016/S0749-6419(00)00012-7">https://doi.org/10.1016/S0749-6419(00)00012-7</a>
- [49] Hartl DJ, Lagoudas DC (2009) Constitutive modeling and structural analysis considering simultaneous phase transformation and plastic yield in shape memory alloys. Smart Mater Struct 18:104017. <a href="https://doi.org/10.1088/0964-1726/18/10/104017">https://doi.org/10.1088/0964-1726/18/10/104017</a>
- [50] Churchill CB, Shaw JA, Iadicola MA (2009) TIPS AND TRICKS FOR CHARACTERIZING SHAPE MEMORY ALLOY WIRE: PART 2-FUNDAMENTAL ISOTHERMAL RESPONSES. Experimental Techniques 33:51–62. <a href="https://doi.org/10.1111/j.1747-1567.2008.00460.x">https://doi.org/10.1111/j.1747-1567.2008.00460.x</a>

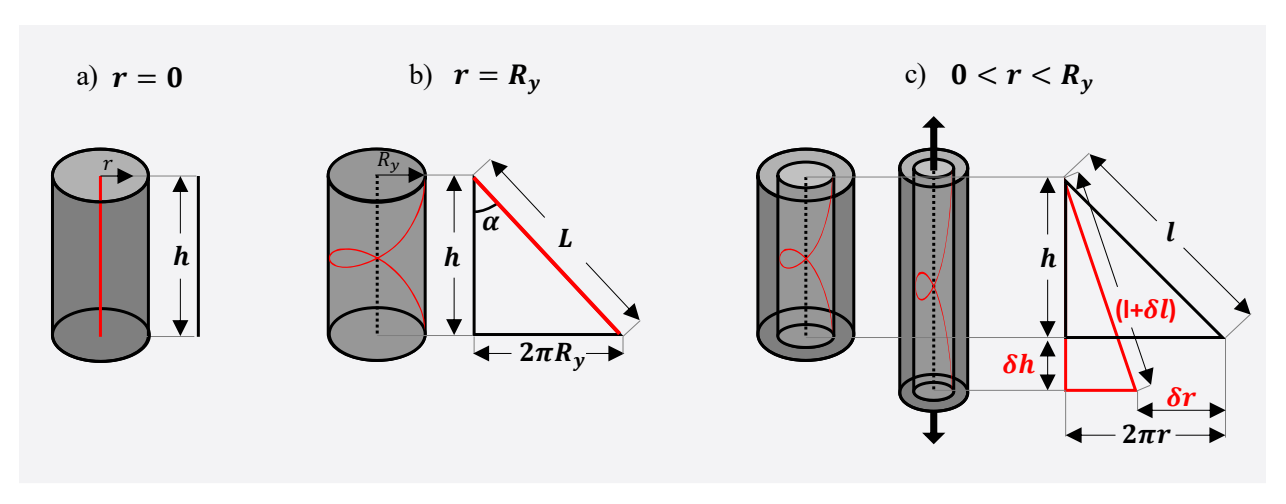


Figure 1. Geometric representation of a microfilament in the center (a), surface (b), and intermediate (c) locations of an idealized yarn structure. The filaments are represented in their helical structures within the yarn cylinder with a shared helical pitch, h, and in the unraveled right triangle forms with their unique radius, r, and length in one turn of twist, l. The impact of yarn extension on the filament geometry is demonstrated in (c).

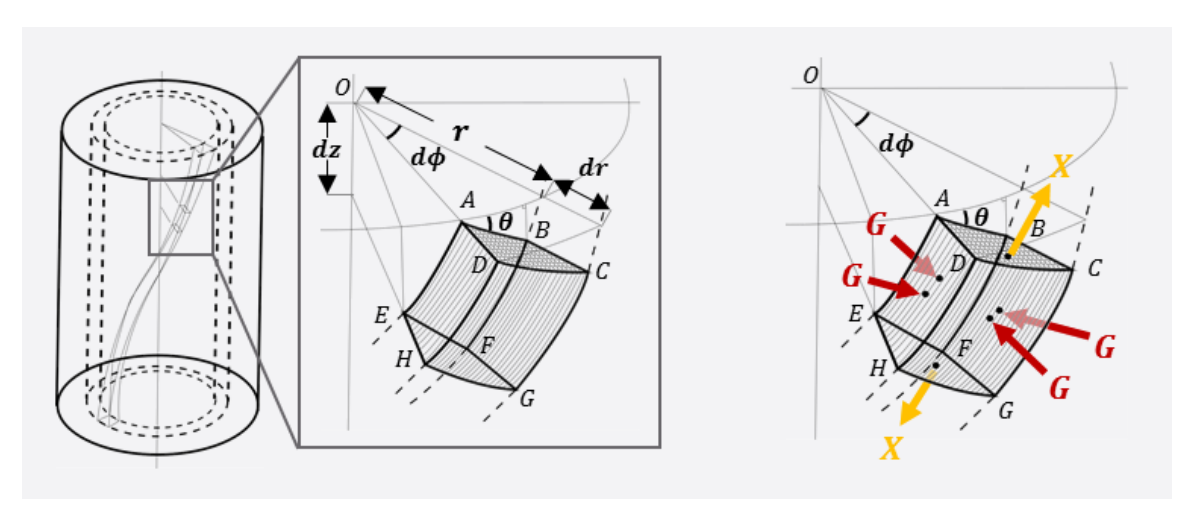


Figure 2. Visual representation of a yarn element at a radial distance, r, and with helical angle,  $\theta$  (left). The element consists of a large number of infinitesimally small microfilaments and is geometrically defined by a radial thickness, dr, an angular change,  $d\phi$ , and a length, dz, within the yarn. During yarn extension, the yarn element experiences an axial stress, X, on the axial faces, ABCD and EFGH, and tangential compression, G, on the remaining transverse faces (right) forming a hydrostatic loading condition.

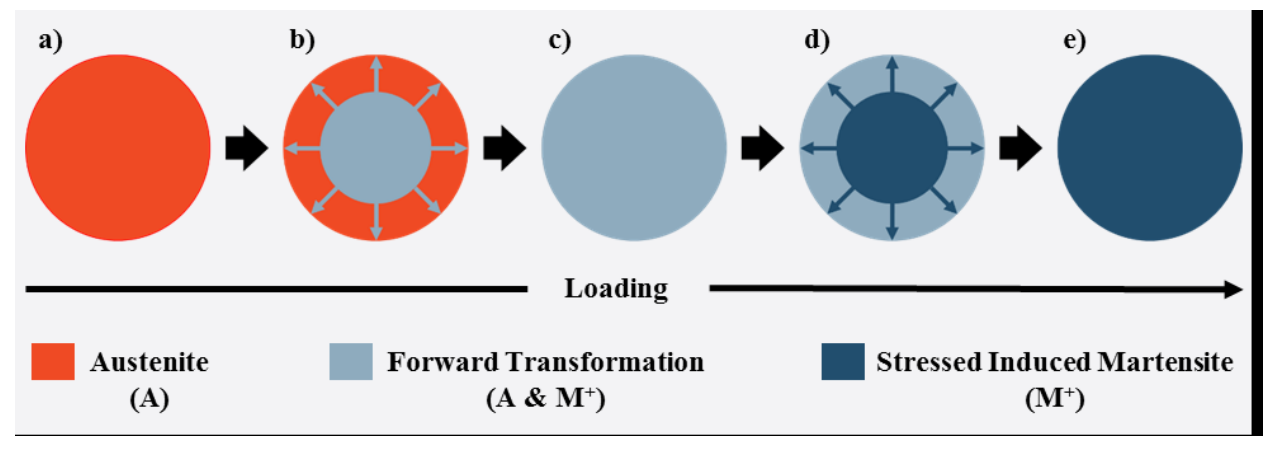


Figure 3. A common material phase evolution of the yarn cross-section during yarn loading at temperatures above austenite finish,  $A_f$ . The yarn starts in a homogeneous austenitic state (a). Forward transformation initiates in the center of the yarn and grows outward (b) until the yarn is in a homogeneous forward transformation (c). Upon further loading, the element in the center of the yarn first completes the forward transformation to SIM (d) and the SIM front grows outward (d) until the entire yarn is in SIM (e).

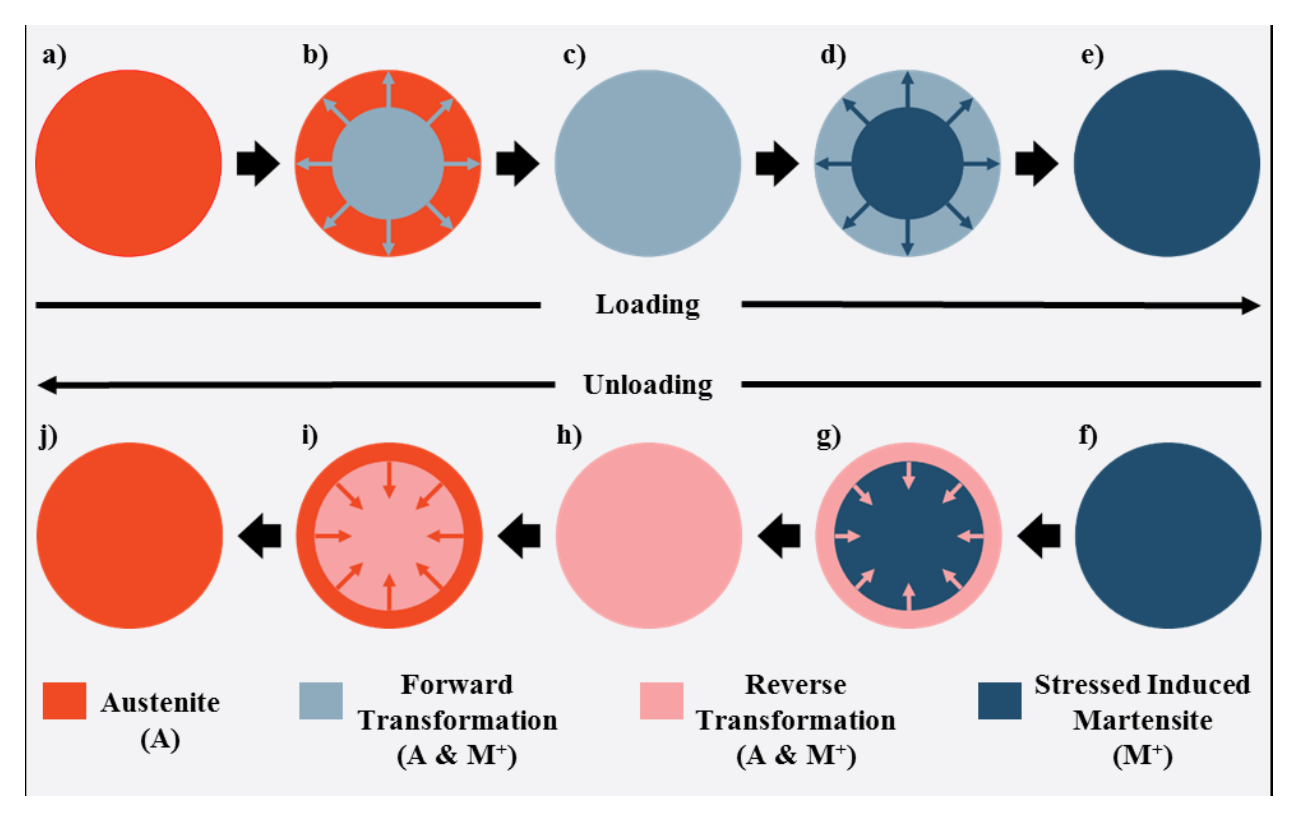


Figure 4. Material phase unloading evolution (f-j) from austenitic loading to a homogeneous SIM yarn state (a-e). At the onset of unloading, the material is in a homogeneous SIM state (f) before reverse transformation initiates on the surface of the yarn (g) and grows inward towards the center of yarn until a homogeneous reverse transformation is reached (h). Reverse transformation back to austenite finished first on the surface of the yarn and grows inward (i) until the yarn is in a homogeneous austenitic state (j).

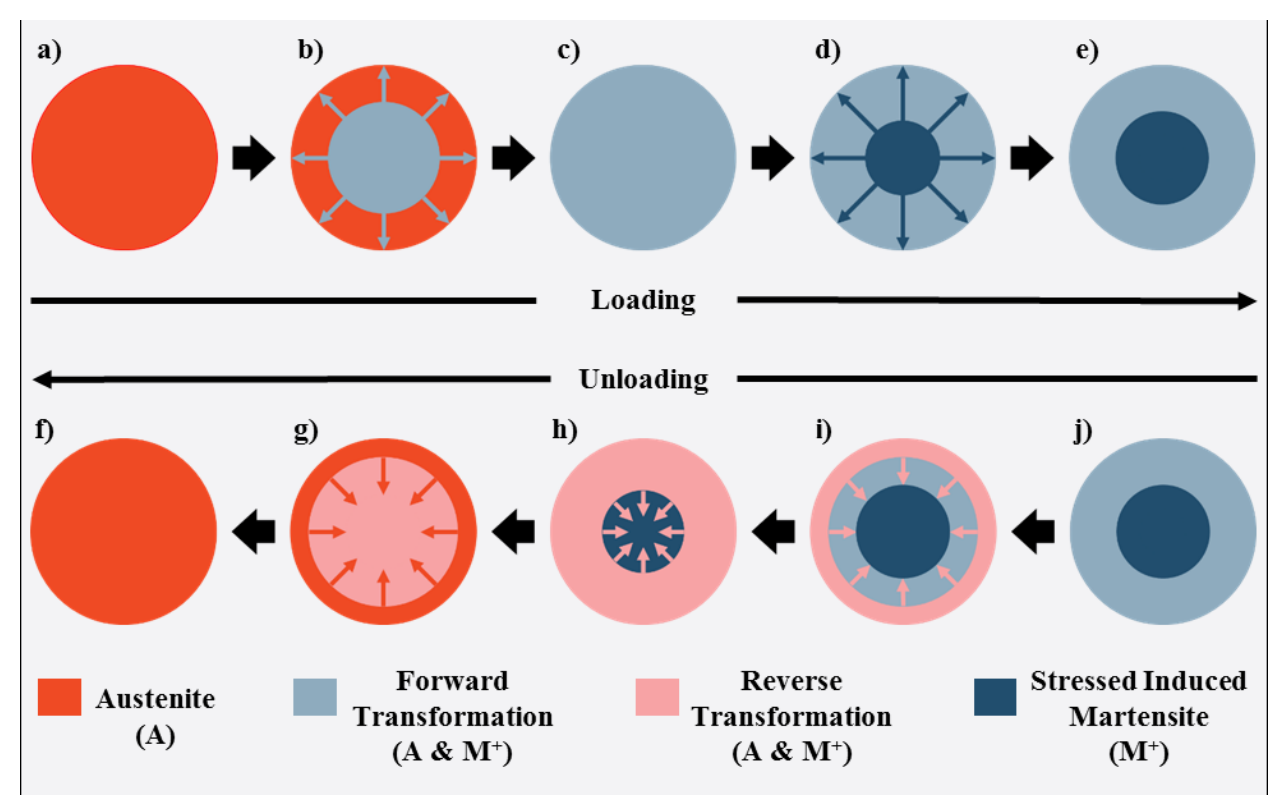


Figure 5. An alternate material phase unloading evolution (f-j) from austenitic loading to a heterogeneous forward transformation and SIM state (a-e). In this unloading evolution, the yarn begins unloading in a heterogeneous state of incomplete forward transformation and SIM (f). In this scenario, the reverse transformation initiates on the surface of the yarn and grows inward (g) through the incomplete forward transformation to the SIM portion of the yarn (h). Upon further loading, the reverse transformation back to austenite will first complete on the surface of the yarn and grow inward (i) until the entire yarn is in homogeneous austenite (j).

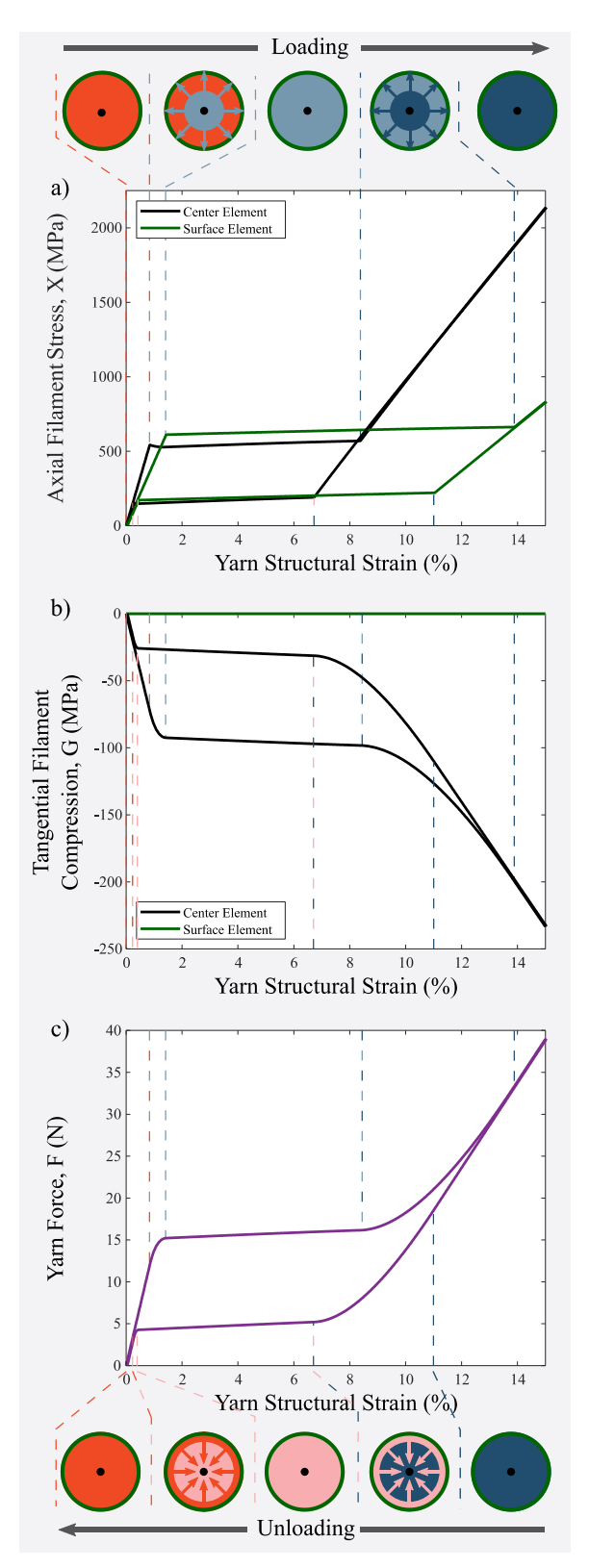


Figure 6. The axial filament stress (a), tangential filament compression (b) loading and unloading response for the center element (black), and surface element (green) of a 6.32 TPCM twisted yarn with 400 filaments of 10µm diameters subjected to a loading displacement of 15.0% structural strain. The correlating global yarn force response is exhibited in (c). The material phase evolution outlined in Figure 4 is used to break up the responses into the correlating homogenous and heterogeneous states.

Material Constants	Values	Material Constants	Values
$E^A$	70.0 <i>GPa</i>	$ ho \Delta s_0^A$	-0.322 MPa
$E^{M}$	25.0 <i>GPa</i>	$ ho \Delta s_0^M$	-0.386 MPa
$ u^A =  u^M$	0.33	Н	0.0585
ρ	$6.45 \frac{g}{cm^3}$	$A_f$	47.8°C
$k^M$	$6.60 \frac{MPa}{^{\circ}C}$	$A_s$	38.62°C
$k^A$	$5.50 \frac{MPa}{^{\circ}C}$	$M_f$	−34.53°C
		$M_{\scriptscriptstyle S}$	−25.12° <i>C</i>
Yarn Constants	Values		
$\overline{v_y}$	(-)0.5		_
С	202.63 tex		
β	0.70, 3.51, 5.27, 7.03, 10.54 <i>TPCM</i>		
arphi	0.45		

Table 1. Material and yarn parameter values used in all simulations. The majority of material values are experiementally derived from a combination of DSC, as well as isothermal uniaxial tensile tests on the 0.70 TPCM yarn. The yarn constants are a combination of manufacturing decisions and values derived from SEM characterization.

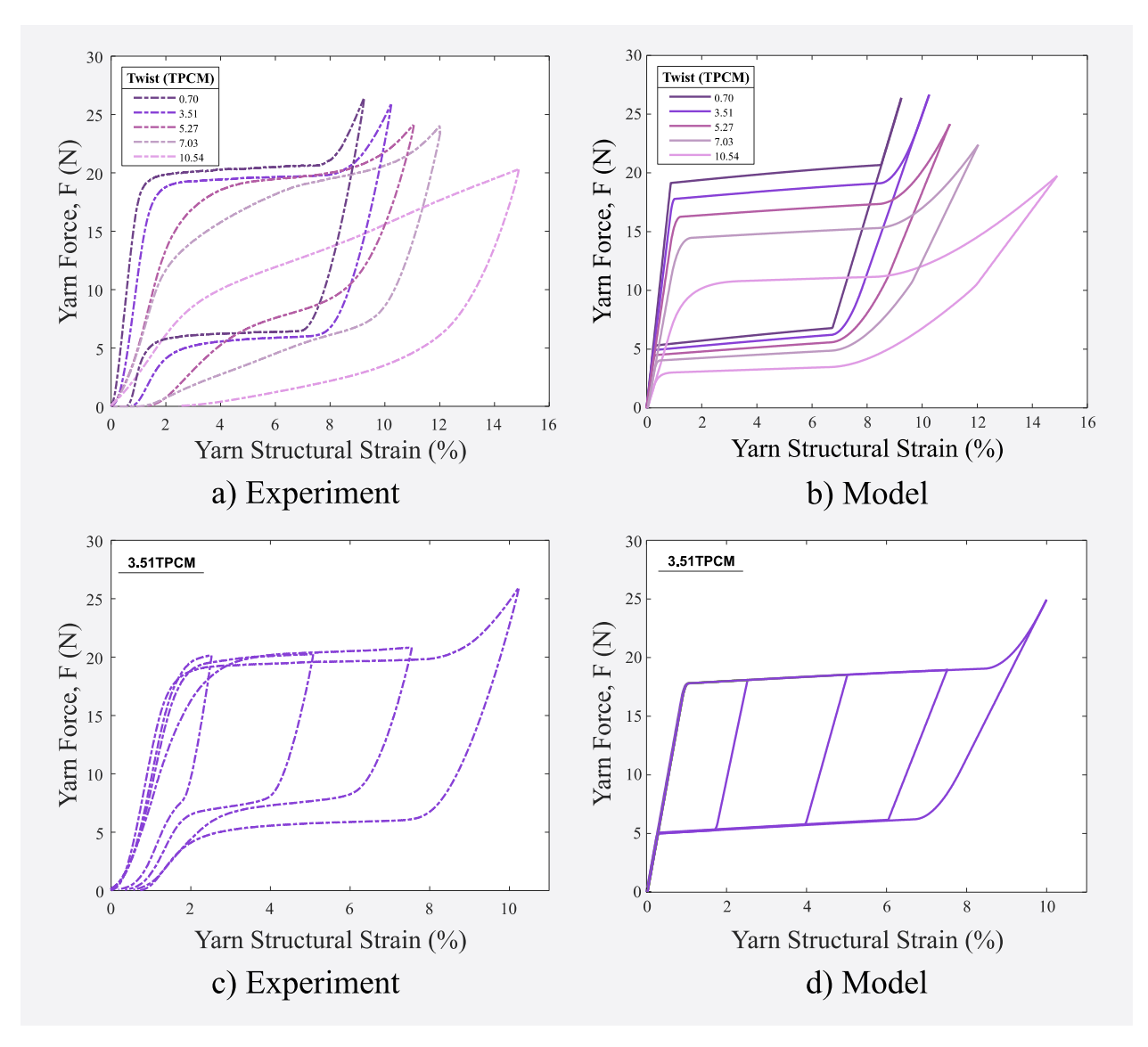


Figure 7. (a) Experimental results of isothermal loading of five yarn configurations of varying twists at temperatures above austenite finish,  $A_f$ . The same yarn configurations and loading conditions are used as inputs in the semi-analytical model to compare the experimental response to the model response (b). The model captures the relationship between twist and effective modulus and transitional regions between phases, but could quantitatively be improved by accounting for early structural strain (1-2%) behavior. (c) Experimental results of isothermal loading of 3.51 TPCM yarns to increasing structural strains to highlight the different unloading behavior from phase evolution yarn stages. (d) Modeling simulations of a 3.51 TPCM yarn loaded to various increasing structural strains to demonstrate the ability to capture different unloading behaviors from phase evolution yarn stages.

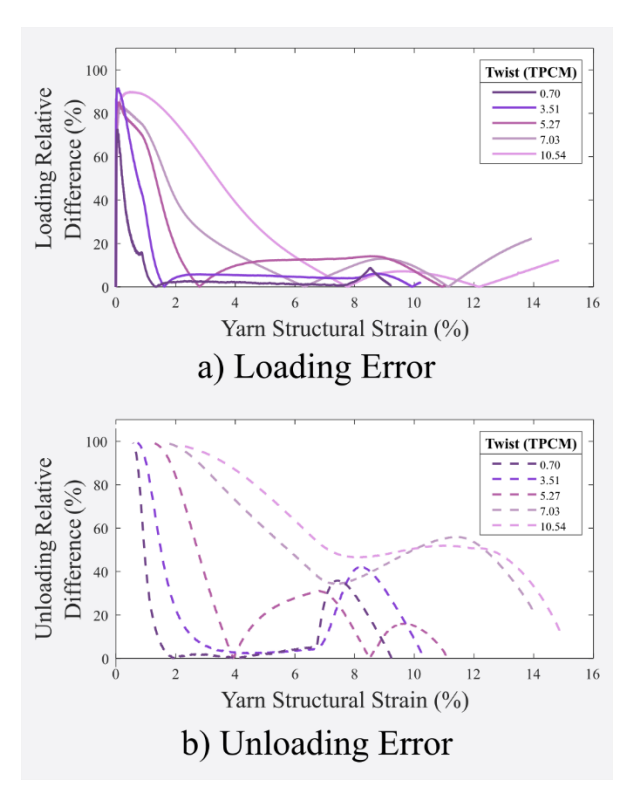


Figure 8. The loading (a) and unloading (b) percent relative difference between the experimental yarn force response (Figure 7a) and modeled yarn force response (Figure 7b). Percent relative difference is observed to be at maximums in early structural strain regions (1-2%), and towards the end of loading (8-14%).